



Fermi National Accelerator Laboratory  
Technical Division / Development & Test Dept.  
PO Box 500 MS 316  
Batavia, IL 60510  
FAX : 630.840.2383

## Calibration of Fixture for Bi-axial Loading of Epoxy Impregnated Nb<sub>3</sub>Sn Cable Ten-Stack, using Epoxy, G10, and Aluminum Samples

R. Conway, G. Ambrosio, P. Bauer, D. Chichili, L. Elementi, and J.-M. Rey<sup>1</sup>  
Technical Division/Development and Test Department

Abstract: Calibration of a new fixture for bi-axial mechanical loading measurements was performed with the use of epoxy, G10, and aluminum test samples. Measurement problems were analyzed, quantified, and eliminated when possible. The samples' mechanical properties, including Young's modulus and Poisson ratio, were measured—at room temperature and liquid helium temperature—as well as their integrated thermal contraction values, with deviations of 0-20% from accepted values. The system was sufficiently understood that measurements could proceed on real Nb<sub>3</sub>Sn cable ten-stacks with full confidence in the experimental results.

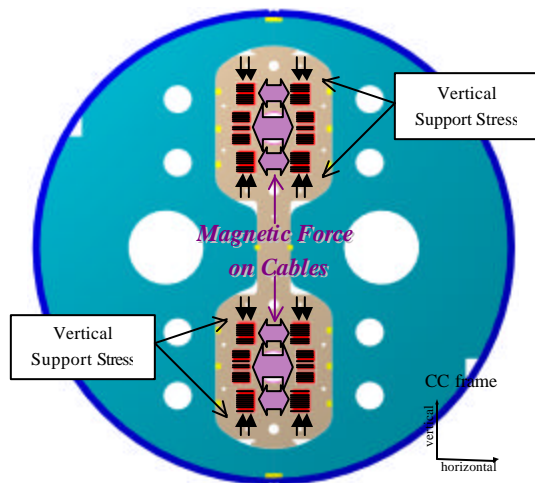


**Figure 1** The CC design produces strong stresses upon the weak horizontal axis of the Nb<sub>3</sub>Sn super-conducting cables (in red), thus requiring supporting stresses in the vertical direction to prevent mechanical failure of the cable.

The common coil (CC) model for 10 T super-conducting dipoles, presently in development at Fermilab TD as part of the VLHC magnet research and development, employs an entirely new structural design.<sup>2</sup> This untested design gives rise to a host of mechanical unknowns, which must be determined in a series of studies in order to ensure structural integrity of the magnet throughout assembly, cooling, and operation. Foremost among these factors are the Young's modulus ( $E$ ), the Poisson ratio ( $\nu$ ), and the integrated thermal contraction ( $\epsilon_{\Delta T}$ ), from  $T = 300$  K to  $T = 4.2$  K, of the epoxy impregnated ten-stack of insulated Nb<sub>3</sub>Sn super-conducting cable, since these variables determine critical mechanical design features for maintaining precise coil configuration throughout the magnet's construction, cooling, and excitation, which itself is essential for achieving high field quality. The CC design entails a bi-axial stress unlike that applied in the traditional cos-theta model (see Figure 1). We

<sup>1</sup> J.-M. Rey is with DAPNIA CEA, Saclay, France.

<sup>2</sup> See G. Ambrosio et al., "Design and development of Nb<sub>3</sub>Sn single-layer common coil dipole magnet for VLHC" to be published in the Proc. of PAC 2001, Chicago, June 2001.

have undertaken a study of this characteristic loading on cable samples so as to conclusively determine these variables.

The study consists of warm and cold measurements of  $E$  and  $\nu$  in epoxy-impregnated Nb<sub>3</sub>Sn cable ten-stacks under uni-axial and bi-axial loads, with the particular final goal of measuring the cable's modulus in the horizontal direction (CC frame) while supported by a vertical pre-stress. This paper describes our calibration of the measurement apparatus for this study, including, in particular, the special fixture made to duplicate the bi-axial stress found in the CC model. The goal of the calibration was repeatable measurements of  $E$  and  $\nu$  for epoxy, G10, and aluminum test samples under this characteristic stress. Since  $E$  and  $\nu$  are well established for these materials, these measurements enable us to determine the accuracy of our measurement apparatus in this particular mechanical test.

<i>Material</i>	$E_{[T=300\text{ K}]} \text{ (MPa)}$	$E_{[T=4.2\text{ K}]} \text{ (MPa)}$	$\nu$
Epoxy	4,300	—	0.33
G10	25,000	31,250	0.33
Aluminum	70,000	85,000	0.33
Copper	150,000	120,000	0.33
Stainless Steel	210,000	225,000	0.33

**Table 1** Expected  $E$  and  $\nu$  values for our calibration materials (test fixture made of stainless steel). No cold measurement was made for the epoxy sample, since the material could not withstand the cooling process.

## UNI-AXIAL LOAD TESTS

### A. Warm Measurement

#### I. Experimental Model

We measured  $E$  and  $\nu$  of the samples by measuring axial ( $\epsilon_a$ ) and lateral strain ( $\epsilon_l$ ) as a function of applied axial stress ( $\sigma_a$ ) in the elastic region of the material, where the relation is linear, and then calculating the desired values according to the following relations:

$$E = \frac{\sigma_a}{\epsilon_a} \tag{1}$$

$$\nu = -\frac{\epsilon_l}{\epsilon_a} \tag{2}$$

where  $\epsilon_l > 0$  (tensile stress) and  $\epsilon_a < 0$  (compressive stress).

The applied stress was provided by a hydraulic load cell, consisting of a hydraulic pump which drives a steel piston, as schematized in Appendix 1. The steel piston makes contact with a 1.750 inch  $\times$  0.570 inch surface steel ram, whose vertical height we extended with a steel block to achieve sufficient height to reach the piston. Stress was measured by the load cell (by strain gauges in the load cell itself) in units of psi and converted to units of MPa. Stress was applied to the samples in a range of  $0 \text{ MPa} < \sigma_a < 60 \text{ MPa}$ .

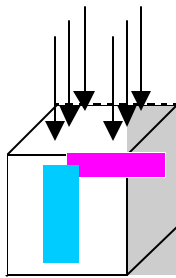


**Figure 2** Cross-wise strain gauge configuration on test sample.

Axial strain and lateral strain were measured with two resistive strain gauges (Micro-Measurements model WK-09-125AD-350) which were affixed to opposite sides of the test samples with Micro-Measurements 200 M-bond glue, one oriented in the axial direction, the other oriented in the lateral direction. These gauges register variable resistance values as they are shortened and elongated along the sample's axes of compression and expansion. The strain, which is

defined as

$$\mathbf{e} = \frac{L - L_0}{L_0} \quad (3)$$

where  $L$  is the length along the relevant axis and  $L_0$  is the initial length (before deformation), is calculated by multiplying the proportionate “resistive strain” by a gauge factor specific to the gauge model and provided by the manufacturer

$$\mathbf{e} = \frac{R - R_0}{R_0} \times \frac{1}{G} \quad [G_{[T=300K]} = 2.07] \quad (4)$$

Even with a clear and simple experimental design for measuring the  $E$  and  $\nu$  values of our samples, we expected mechanical peculiarities of the measurement apparatus to yield imperfect results, thus requiring a “debugging” of the system. This debugging process will be detailed in the discussion of our results.

## II. Measurement Apparatus and Procedure

*Preparation:* The sample is placed centrally in the test bed of a specially designed fixture (see Fig. 3), which consists of two robust stainless steel disks of radius 2.9375 inches—a 2.287 inch thick base which houses the 2.000 inch  $\times$  1.762 inch test bed, and a 1.500 inch top, containing ten screw holes for the connecting bolts; a rectangular aperture in the fixture top gives the steel ram access to the sample housed in the base.<sup>3</sup> The wire leads from the strain gauges are lead from the fixture through holes in the test bed and affixed in a specially cut groove to the underside of the fixture base with soft putty, so as to prevent slicing the wires on the fixture’s sharp edges as it is moved about. The fixture top is bolted to the

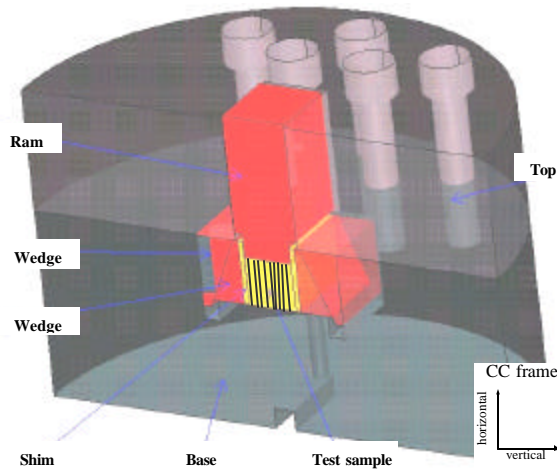


**Figure 3** Cross section of test fixture, including top plate (with bolts) and base, loading ram (red), and test bed. The test sample (yellow) sits inside the test bed, and during biaxial loading, is pre-stressed in the vertical (CC frame) direction by the fixture’s vertical stress mechanism (explained below in our discussion of the biaxial load test). Note: the elements for this vertical stress mechanism are not included in the uniaxial load test set-up.

base with ten cobalt-hardened steel bolts, and the fixture is positioned at the center of the load cell base. The steel ram is set upon the sample through the aperture of the fixture top, with the steel ram extension attached with tape along the sides so that no tape lies within the line of force. The wire leads are fed through a groove in the left side of the load-cell base, which is then lifted (with a foot pump) and bolted to the main cylinder of the load-cell, providing a rigid base upon which the load-cell piston may apply its pressure. The eight wire leads (four from each gauge) are connected in series to a circuit with a constant applied current, on the exterior of the load cell cylinder. As the strain gauge resistance changes during loading, the circuit voltage changes, enabling measurement of the resistance change.

*Measurement:* The circuit, which passes through a channel scanner and a voltmeter, is monitored by a Labview program (filename: R-LC\_Cal01.vi), newly designed for this project, which both operates the piston and reads the stress and resistance values at regular stress intervals

<sup>3</sup> Pierre Bauer et al. “Test Fixture for Mechanical Ten-Stack Measurements for the Common Coil Dipole Model Magnet”. Fermilab Technical Division Internal Note TD-00-040, June, 2000. The fixture’s design is primarily constructed to meet the mechanical demands of the bi-axial load tests.

throughout the experiment.<sup>4</sup> When initializing the measurement, we input 1) dimensions of the sample's pressure receiving surface, 2) maximum desired load, and 3) the filename to which the data is to be written. Before taking measurements, the sample is put through a message sequence which "trains" the sample-and-gauge composite to respond consistently to the applied load. This message sequence consists of 5 cycles of loading and unloading the sample between zero and maximum load. After massaging the sample, we proceed with the measurement sequence (select the "calibration" setting in the program), measuring resistance from both gauges automatically at intervals of  $\sigma_a = 500$  psi in a range of  $0 \text{ psi} < \sigma_a < 9000$  psi, through three load-unloading cycles. After conducting a first measurement, designated Test 1, the sample is rotated 90 degrees about the axis between the two gauges, and an identical measurement is taken in the new orientation, designated Test 2. This procedure enables us to test gauge specific effects upon the data.

### III. Data and Results

*Data Analysis:* The Labview program outputs a data set of pressure (i.e. stress) values, measured in psi, and resistance values, measured in ohms. Stress values are converted from psi to MPa. Strain values are calculated from the resistance values according to the above equation. The data is plotted against the expected values predicted by the theory (Equations 1 and 2) and the accepted values in Table 1, and the graphs are off-set (translated vertically) by a fixed value, in order to set the graphs at their true zero point, as suggested by trends in the data.

*Results:* Our initial data yielded a negative strain in the gauge parallel to the axis of compression and positive strain in the gauge perpendicular to the axis of compression, both varying linearly with pressure, as expected; however, the measurements lacked precision.

Several observations and tests suggested a variety of elasticities in the system as a source of anomalies in our measurement results. These sources of error, and their respective corrections, by changes to the experimental set-up and by means of data analysis, are discussed extensively in Appendix 2. Among them, the data "fork rotation" in the first series of measurements lead to the introduction of a new method for securing the sample's position within the fixture, using a "tape frame" surrounding the base of the sample, rather than the layer of double-sided tape underneath the sample which was originally used for this purpose. Another problem, a consistently present initial offset in the data justified our introduction of an off-set correction; this correction was required to make even our best results comply with the expected values.

With these corrections made, our measurements generated data in good compliance with our theoretical predictions. Figure 4 shows our best results for warm uni-axial loading.

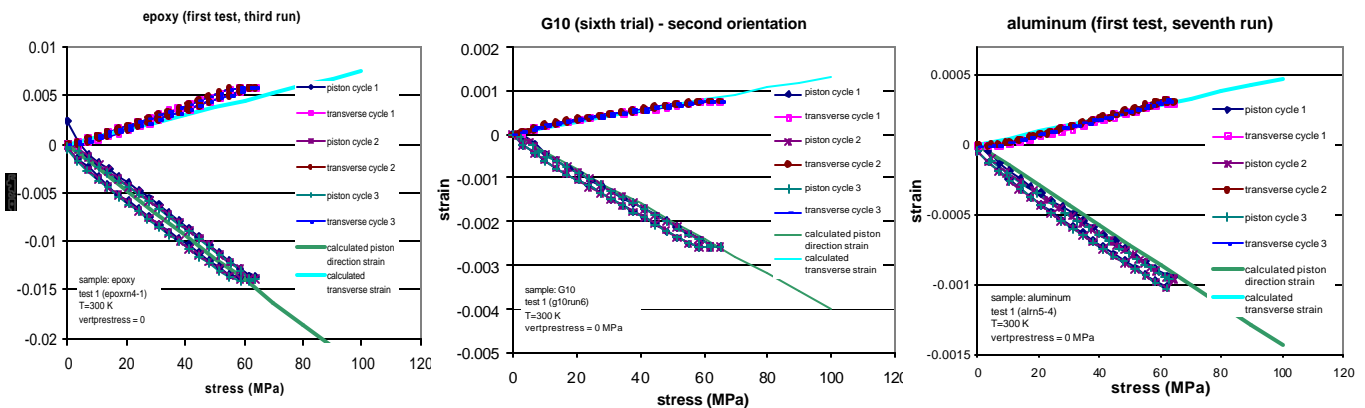


**Figure 4** Best results for warm uni-axial loading of epoxy, G10, and aluminum samples.

<sup>4</sup> Program designed by T. Wokas and M. Whitson, with an outside consultant. Capacitance gauge reading capability was added by L. Elementi.

With our corrections generating good measurements, such as those displayed in Figure 4, we could calculate E and  $\nu$  values which were truly representative of the samples' mechanical properties. The modulus was calculated from the slope of the linear region of the axial strain data (loading phase rather than unloading phase) for the second or third loading cycle (since the first cycle usually exhibited a larger distorting hysteresis than the second and third). Derivative plots (see Appendix 2, Figure 9) were employed to rigorously establish the stress range of the linear strain data. The E values calculated from our measurements, for the three samples, are plotted against the accepted values in Figure 5. We also calculated the Poisson ratio of our samples from our data by selecting 10 point pairs within the linear region of the data from a fully corrected measurement (including all appropriate offset corrections, which are critical for this calculation), and calculating the ratio according to Equation 2. All of the calculated E and  $\nu$  values, for the epoxy, G10, and aluminum samples, are listed in Table 1 of Appendix 3. As expected, the systematic statistical error for this measurement increased as the test sample modulus approached the intrinsic modulus of the measurement apparatus. The precise error dependence on modulus is given by

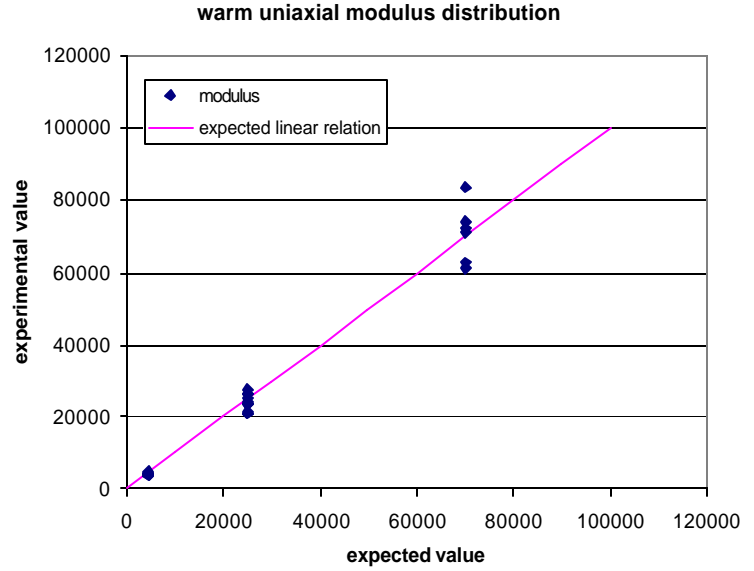


**Figure 5** Plot of modulus values calculated from good warm uniaxial loading tests on epoxy, G10, and aluminum samples vs. expected values.

$$|\Delta E| = 0.0000005 E^2 + 0.0792 E \quad (5)$$

Our final mean measured values for E and  $\nu$  in warm uniaxial loading were in good compliance with the accepted values. The mean measured value of  $E_{\text{epoxy}} = 4,216.84 \pm 336.75$  MPa, which has a 1.93% deviation from the accepted value of 4,300 MPa; the mean measured value of  $E_{\text{G10}} = 23,758.15 \pm 2,312.33$  MPa, which has a 4.97% deviation from the accepted value of 25,000 MPa; and the mean measured value of  $E_{\text{aluminum}} = 70,764.20 \pm 8,120.77$  MPa, which has a 1.09% deviation from the accepted value of 70,000 MPa. The mean measured value of  $\nu_{\text{epoxy}} = 0.477 \pm 0.116$ , which has a 44.42% deviation from the accepted value of 0.33; the mean measured value of  $\nu_{\text{G10}} = 0.348 \pm 0.179$ , which has a 5.39% deviation from the accepted value of 0.33; and the mean measured value of  $\nu_{\text{aluminum}} = 0.346 \pm 0.075$ , which has a 4.91% deviation from the accepted value of 0.33.

## B. Cold Measurement

### I. Experimental Model

The essential elements of the experimental model for the measurement of the samples' mechanical properties during cold uniaxial loading remained the same as for the warm measurement. In contrast to the warm measurement, which was conducted at room temperature, the cold measurement was conducted at 4.2 K by cooling the entire measurement system with liquid helium. Since the epoxy sample could not withstand the stresses associated with such cooling, only G10 and aluminum samples were used for the cold measurement. E and  $\nu$  were calculated as before from Equations 1 and 2, though the

expected E values were different, since the materials' mechanical moduli increase as temperature decreases. The expected modulus values for our samples at 4.2 K were  $E_{G10} = 31,250$  MPa and  $E_{\text{aluminum}} = 85,000$  MPa. The gauge factor, employed in the calculation of mechanical strain from the strain gauge resistance values, according to Equation 4, was also different at 4.2 K, increasing to  $G_{[T=4.2\text{ K}]} = 2.15$ .

In addition, after cooling the sample—before our mechanical tests at 4.2 K—we calculated the sample's integrated thermal contraction  $\epsilon_{\Delta T}$ , over the change in temperature,  $\Delta T = 300\text{ K} - 4.2\text{ K} = 295.8$  K; we calculated this quantity from the thermal strain registered by the strain gauges following cool-down. Just as a mechanical strain of the sample proportionately strains the attached strain gauge from its natural equilibrium length at the given temperature (the principle by which we relate the “resistive strain” of the strain gauge to the mechanical strain of the sample), so the difference in thermal strains between the gauge and the sample over a given temperature range produces an effective mechanical strain on the strain gauge from its natural equilibrium length at the new temperature, which is registered by a shift from the natural equilibrium resistance of the gauge. Thus, for a strain gauge bonded to the surface of a test sample with different  $\epsilon_{\Delta T}$  from that of the gauge, the resulting thermo-mechanical strain of the gauge is given by

$$\begin{aligned} \Delta e_{\Delta T \text{ gauge-sample}} &= e_{\Delta T \text{ gauge}} - e_{\Delta T \text{ sample}} & (6) \\ &= \frac{R_{0T=4.2K} - R_{0T=300K}}{R_{0T=300K}} \times \frac{1}{G_{\Delta T \text{ avg}}} \quad [G_{\Delta T \text{ avg}} = 2.11] \end{aligned}$$

Material	$e_{DT}$ (mm/m)
Stainless Steel	3.05
Copper	3.30
Aluminum	4.40
G10*	2.73

**Table 2** Accepted values of integrated thermal contraction ( $\epsilon_{\Delta T}$ ) for select materials. \*Value listed for G10 is thermal strain in “low shrinking” direction (along plane of fiber-glass sheets).

where we have taken for  $G_{\Delta T \text{ avg}}$ , the gauge factor over the temperature range, the average of the two boundary values,  $G_{[T=300\text{ K}]} = 2.07$  and  $G_{[T=4.2\text{ K}]} = 2.15$ . Since the Micro-Measurements model WK-09-125AD-350 gauge which we employed has an  $\epsilon_{\Delta T}$  equal to that of stainless steel, we substituted the known value of  $\epsilon_{\Delta T \text{ steel}}$  for  $\epsilon_{\Delta T \text{ gauge}}$  in Equation 6 and, combined with our measured value of  $\epsilon_{\Delta T \text{ gauge-sample}}$ , calculated the measured integrated thermal contraction of the sample by

$$e_{\Delta T \text{ sample}} = e_{\Delta T \text{ steel}} - \Delta e_{\Delta T \text{ gauge-sample}} \quad (7)$$

Some values of the integrated thermal contraction relevant to our measurement are listed in Table 2.

## II. Measurement Apparatus and Procedure

*Preparation:* Before cooling to cryogenic temperatures for a measurement, each instrumented sample is thermally “massaged”, in order, like the mechanical massaging which precedes each measurement, to train the sample-gauge composite for consistent response to thermal contraction. This massage consists of thermo-cycling each instrumented sample between room temperature and liquid nitrogen temperature through 5 cycles, alternately freezing it in liquid nitrogen and warming it in the air. This need only be done once in the lifetime of each instrumented sample.

As in preparation for the warm measurement, the sample is first placed in the test fixture, and the fixture is sealed inside the load-cell. A warm measurement is performed through at least two cycles before cooling to establish the loading pattern for the particular experimental set-up and to certify that all significant potential errors (as described in the discussion of the warm measurement) have been avoided. A series of zero-load strain gauge resistance values are measured according to the procedure described in Appendix 4, which, combined with values obtained with identical measurements following cool-down, enable calculation of the sample's integrated thermal contraction.

Next, the entire assembly is prepared for cooling. A 100 liter steel vacuum-insulated liquid helium dewar is raised by the foot pump and bolted to a cover plate, sealing the fixture-housing portion of the load-cell cylinder inside. A wooden plank is wedged underneath the dewar to provide secondary

support. With a liquid helium supply dewar positioned next to the load cell, a transfer line (attached to the liquid helium valve on the supply dewar) is inserted into a hole in the cover plate and tightened around the aperture. After closing the 3 lbs pressure exhaust valve on the supply dewar, a separate hose from a helium gas tank at 3 lbs pressure is connected to the helium gas valve of the liquid helium supply dewar, thus providing the hydraulic pressure needed inside the supply dewar to transfer liquid helium to the load-cell dewar. Opening the valves to the helium lines, liquid helium transfer proceeds and is monitored by a liquid-level gauge on the instrument stack next to the load-cell. Liquid helium does not begin accumulating in the dewar until after one and a half hours of transfer, since the warm system evaporates the cold liquid rapidly during the initial phase of cooling. When liquid begins to accumulate, the pre-measurement mechanical massage sequence may be performed. Once a liquid level of 25% is reached, ensuring that the entire fixture is submerged in liquid helium (which is required for liquid to reach the sample, since the only open passage to the sample is through the slot in the fixture cover plate), the second set of zero-load strain gauge resistance values is measured.<sup>5</sup> Piston loading may then proceed, though liquid helium transfer continues until reaching a liquid level sufficient to ensure submersion of the fixture throughout the desired number of measurements (liquid helium cannot easily be added to the system once transfer has ceased, because the transfer pipes become warm and must be recooled). Since liquid level is lost during measurement at a rate of 0.5% per minute, a level of 50-60% is desirable for 2-3 measurements. Once the desired level is achieved, the open valves on the supply dewar are closed and the closed exhaust valve is opened to avoid a dangerous pressure build-up inside the sealed dewar.

*Measurement:* The procedure for a cold uni-axial loading test is identical to that of the warm measurement, though only one orientation of the sample can be tested for each cooling of the system.

*Disassembly:*<sup>6</sup> After the measurement is completed, the load-cell dewar is unbolted from the cover plate and the support plank is removed. The dewar is lowered very, very slowly by gently releasing the foot pump, thereby allowing time for the liquid helium inside the cylinder to be evacuated through holes in the bottom. Once completely lowered, the dewar is covered to help control liquid helium evaporation. The load cell base is unbolted and lowered according to standard procedure, to expose the fixture to the warm air, and a set of fans are switched on, to facilitate heat transfer about the system. The system is left to warm overnight, before it can be used again. Thus, only one cold measurement may be conducted during each 24 hour period.

### III. Data and Results

*Data Analysis:* The integrated thermal contraction is calculated according to Equations 6 and 7, combining the accepted value for  $\epsilon_{\Delta T \text{steel}}$  listed in Table 2 with the averaged zero-load strain gauge resistance values measured immediately before and after cooling. The full set of values involved in this calculation is listed in Table 4 of Appendix 3. Data analysis for calculation of the samples' mechanical properties—Young's modulus and the Poisson ratio—measured in the cold uni-axial loading test is the same as for the warm test, though employing the new values indicated above.

*Results:* No significant problem was encountered with measurement of the thermal strain. The mean measured values of our samples' integrated thermal contraction are listed in Table 3.

<i>material</i>	<i>mean measured <math>\epsilon_{DT}</math> (mm/m)</i>	<i>st. dev.</i>	<i>theory <math>\epsilon_{DT}</math> (mm/m)</i>	<i>deviation from theory</i>
G10	2.40	0.84	2.73	0.1198
aluminum	5.21	0.11	4.40	0.1843

**Table 3** Measured values of the integrated thermal contraction of G10 and aluminum samples, integrated over the temperature path from room temperature, 300 K, to liquid helium temperature, 4.2 K.

<sup>5</sup> Note: The cold zero-load capacitance and resistance values measured here serve a critical role in the calculation of measured cold vertical pre-stress during the cold bi-axial load test (see Appendix 6). These values are thus important for not only the cold *uni-axial* load test, but also for the cold *bi-axial* load test, which is the last test in a typical measurement program for a sample.

<sup>6</sup> Note: Two people are required to be present during disassembly, for safety purposes.

Our final mean measured values for  $\epsilon_{\Delta T}$ , with  $\Delta T = 300 \text{ K} - 4.2 \text{ K} = 295.8 \text{ K}$ , were in acceptable compliance with the accepted values for the calibration samples. The mean measured value of  $\epsilon_{\Delta T G10} = 2.40 \pm 0.84 \text{ mm/m}$ , which has a 11.98% deviation from the accepted value of 2.73 mm/m, and the mean measured value of  $\epsilon_{\Delta T \text{aluminum}} = 5.21 \pm 0.11 \text{ mm/m}$ , which has a 18.43% deviation from the accepted value of 4.40 mm/m.

One distinct cold load test was performed on the G10 sample, and two distinct tests were performed on the aluminum sample. Our best results for cold uni-axial loading are displayed in Figure 6.

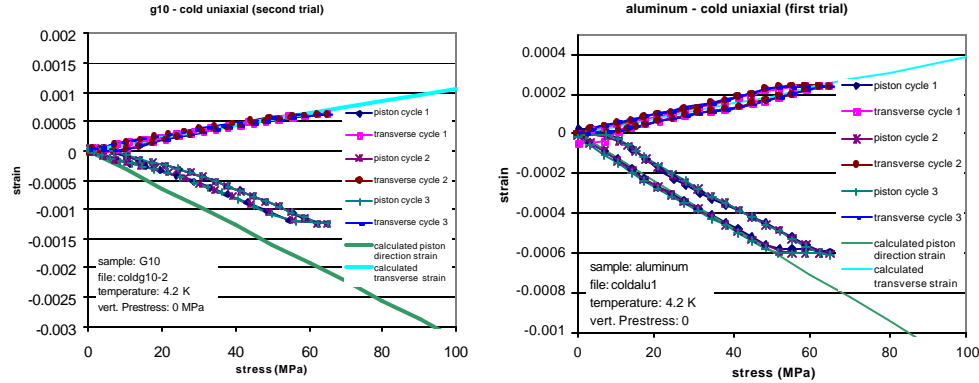


**Figure 6** Best results for cold uni-axial loading of G10 and aluminum samples.

No significant problems were encountered as impediments to calculation of cold E and  $\nu$  values for our samples, since the measurement is mechanically identical to the warm uniaxial load test, whose problems were corrected before proceeding to the cold test. The E values calculated from our measurements, for the two samples, are plotted against the accepted values in Figure 7. The systematic statistical error for this measurement also increased exponentially with modulus, according to the relation

$$|\Delta E| = 79.127 e^{0.00007E} \quad (6)$$

All of the calculated E and  $\nu$  values, for the G10 and aluminum samples, are listed in Table 2 of Appendix 3.

Our final mean measured values for E and  $\nu$  in cold uniaxial loading were in acceptable compliance with the accepted values. The mean calculated value of  $E_{G10} = 38,167.51 \pm 996.37 \text{ MPa}$ , which has a 22.14% deviation from the accepted value of 31,250 MPa, and the mean calculated value of  $E_{\text{aluminum}} = 76,874.64 \pm 12,994.73 \text{ MPa}$ , which has a 9.56% deviation from the accepted value of 85,000 MPa. The mean calculated value of  $\nu_{G10} = 0.607 \pm 0.000$ , which has a 83.84% deviation from the accepted value of 0.33, and the mean calculated value of  $\nu_{\text{aluminum}} = 0.317 \pm 0.075$ , which has a 4.00% deviation from the accepted value.

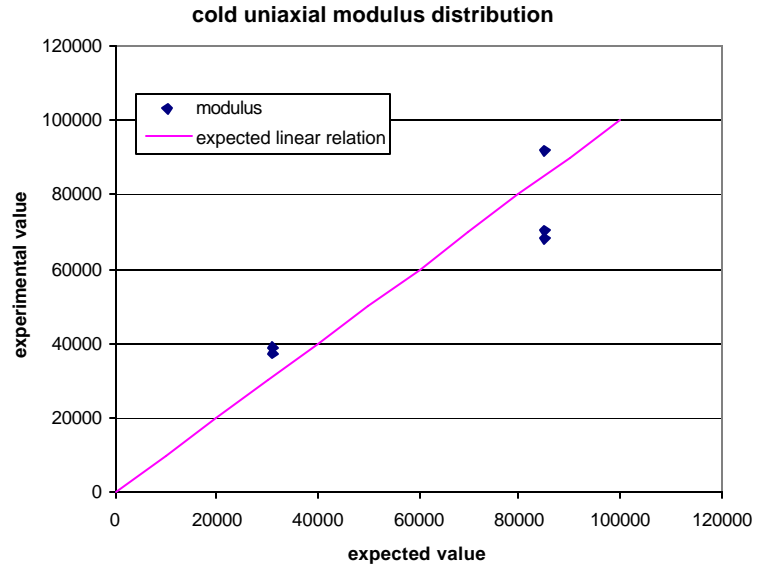


**Figure 7** Plot of modulus values calculated from good cold uni-axial loading tests on G10 and aluminum samples vs. expected values.

## BI-AXIAL LOAD TESTS

### A. Warm Measurement

#### I. Experimental Model

As in the uni-axial loading test, we calculated  $E$  and  $\nu$  of the test samples in the bi-axial loading test as a function of measured stress and strain.<sup>7</sup> With loads applied along both the vertical and horizontal axes of the samples, we have, according to Hooke's Law generalized for multi-axial loading,

$$\mathbf{e}_h = \frac{\mathbf{S}_h}{E_h} - \mathbf{u} \frac{\mathbf{S}_v}{E_v} \quad (7)$$

$$\mathbf{e}_v = \frac{\mathbf{S}_v}{E_v} - \mathbf{u} \frac{\mathbf{S}_h}{E_h} \quad (8)$$

Though the bi-axial Poisson strain merely subtracts a constant factor from the axial strain in each direction, which we removed from our piston-loading data with the conventional offset correction (setting  $\epsilon(\sigma) = 0$  for each axis), Equation 8 defines the magnitude of the effective strain confining the sample to zero vertical strain in the case of an infinitely sufficient vertical constraining force. This confining effect therefore gives us the condition

$$\mathbf{e}_v = \frac{\mathbf{S}_v}{E_v} - \mathbf{u} \frac{\mathbf{S}_h}{E_h} = 0 \Rightarrow \frac{\mathbf{S}_v}{E_v} = \mathbf{u} \frac{\mathbf{S}_h}{E_h} \quad (9)$$

which, when factored into the horizontal strain during piston loading, according to Equation 7,

$$\mathbf{e}_h = \frac{\mathbf{S}_h}{E_h} - \mathbf{u}^2 \frac{\mathbf{S}_h}{E_h} \quad (10)$$

gives rise to a new apparent modulus in the horizontal direction,

$$\mathbf{S}_h = E_{constrained} \mathbf{e}_h, \quad E_{constrained} = \frac{E_{free}}{1 - \mathbf{u}^2} \quad (11)$$

which is greater than the unconstrained, or free, modulus, making the sample appear stiffer under load than it actually is. The horizontal modulus measured under bi-axial loading must therefore be corrected accordingly to determine the real, free-loading (uni-axial) modulus of the sample in the horizontal direction.<sup>8</sup>

Since the test fixture, itself having the finite stiffness of stainless steel, does not provide an infinitely rigid constraint to the sample, the real situation of the bi-axial measurement is an intermediate

---

<sup>7</sup> At this point in the discussion, we switch to the CC reference frame (see Figure 8), which makes more sense for describing the bi-axial loading test. Our "axial" direction, the uni-axial loading axis parallel to the load cell piston, corresponds to the "horizontal" axis in the common coil frame, and the "lateral" direction perpendicular to the uni-axial loading axis corresponds to the vertical axis in the CC frame.

<sup>8</sup> Since calculation of the sample's free horizontal modulus is the concern of this measurement, the bi-axial measurement appears superfluous in the context of homogeneous calibration samples, given that this value is determined, more easily and effectively, by the uni-axial measurement. The need for the bi-axial measurement becomes apparent, however, in the context of composite epoxy impregnated Nb<sub>3</sub>Sn cable ten-stacks, whose free horizontal modulus is the ultimate objective of the measurement, since the ten-stack is highly susceptible to mechanical failure under loading in the horizontal direction, due to its composite structure, unless vertically constrained. Consequently, the only means of measuring the ten-stack's horizontal modulus through horizontal loading is with the addition of a vertical support stress providing sufficient vertical constraint to prevent mechanical failure of the sample.

case between that of free loading and that of the infinitely rigid constraint. We therefore correct the apparent (constrained) modulus with a correction factor

$$E_{constrained} = \frac{E_{free}}{1 - u^2(1 - f)}, \quad f = \frac{E_{sample}}{E_{steel}} \quad (12)$$

This factor gives us the correct boundary conditions. As  $E_{sample} \rightarrow E_{fixture}$ ,  $f$  approaches one and the correction factor approaches zero, setting the apparent modulus equal to the free modulus, since the fixture's resistance to strain, for the given stress, is equal to that of the sample and therefore provides no constraint to the sample. Conversely, for  $E_{sample} \ll E_{fixture}$ ,  $f$  approaches zero and the correction factor approaches one, giving the infinitely rigid constraint condition, the effective result for a large difference between the modulus of the sample and the modulus of the fixture. This model predicts room temperature constrained modulus values for our samples of  $E_{epoxy\_constrained} = 4,813$  MPa,  $E_{G10\_constrained} = 27,653$  MPa, and  $E_{aluminum\_constrained} = 75,480$  MPa.

The confining vertical support stress was applied to the sample through a simple wedge mechanism employed by the fixture, which is illustrated in Figure 8. When bolted into the fixture base, the fixture's top plate drives a protruding upper wedge along the surface of a lower wedge, thus

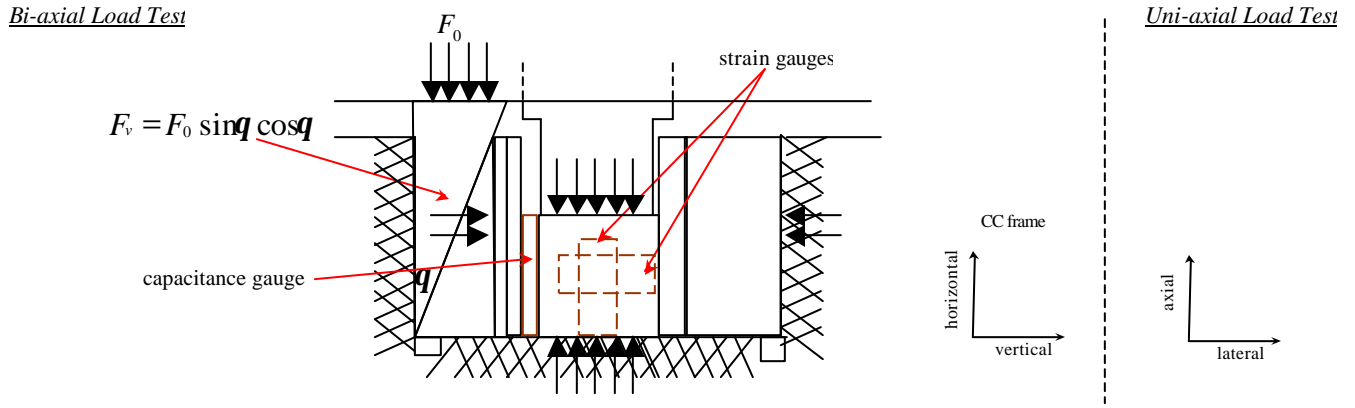


**Figure 8** Bi-axial loading forces in the fixture test bed. Vertical force is applied to the sample through the wedge system inside the test bed.  $F_0$  is applied by the fixture top plate to the top wedge, and the wedge system, with  $\theta = 23^\circ$ , converts approximately half of that force to a vertical force on the test sample. Horizontal force is applied to the test sample directly by the steel ram, which connects to the load cell piston.

transforming a downward pressure to a lateral pressure within the test bed, and this serves as the vertical stress on the sample in the CC frame. The downward force is transformed through the wedge system according to the geometric relation

$$F_v = F_0 \sin q \cos q \quad (13)$$

where  $F_0$  is the initial downward force exerted by the top plate upon the upper wedge,  $F_v$  is the resulting vertical force (CC frame) within the test bed, and  $\theta$  is the wedges' angle of inclination. With an angle of inclination of  $23^\circ$ , 0.36 times the downward force is transformed to a vertical force. The vertical stress was measured with a capacitance gauge, which, when squeezed between the test sample and displaced lower wedge, registers a stress-dependent capacitance; from this capacitance value, a stress could be calculated according to a prior calibration of the gauge at room temperature,

$$C = 0.0003666s + C_0 \quad (CC10SC1)$$

$$C = 0.0003725s + C_0 \quad (CC10SC2)$$

where  $C$  is the capacitance value in nF,  $\sigma$  is the pressure in MPa, and  $C_0$  is a zero load capacitance value determined at the beginning of the measurement. The horizontal stress was applied directly by the load cell piston and read in the same fashion as in the uni-axial loading test.

Vertical and horizontal strain were measured in the same way as in the uni-axial loading test, with resistive strain gauges affixed to the test sample in cross configuration.

## II. Measurement Apparatus and Procedure

*Preparation:* The test fixture is first clamped in a simple preparation fixture, displayed in Figure 9, which secures it against the high bolting torque needed to operate the wedge mechanism. Before being placed in the fixture test bed, the bi-axial loading elements are cleaned, and an acrylic lubricant is applied to the wedge sliding surfaces as well as the fixture surfaces in contact with the wedges so as to prevent friction and metallic bonding between the elements, which can occur at the fixture's high internal pressures. The elements are carefully aligned in the fixture as shown in Figure 10, making certain that they are all perfectly aligned from above and that the capacitance gauge surface, in particular, matches perfectly the sample surface upon which it sits. The co-axial cable from the capacitance gauge is lead out of the fixture and secured through the same passage used for the strain gauge wires.

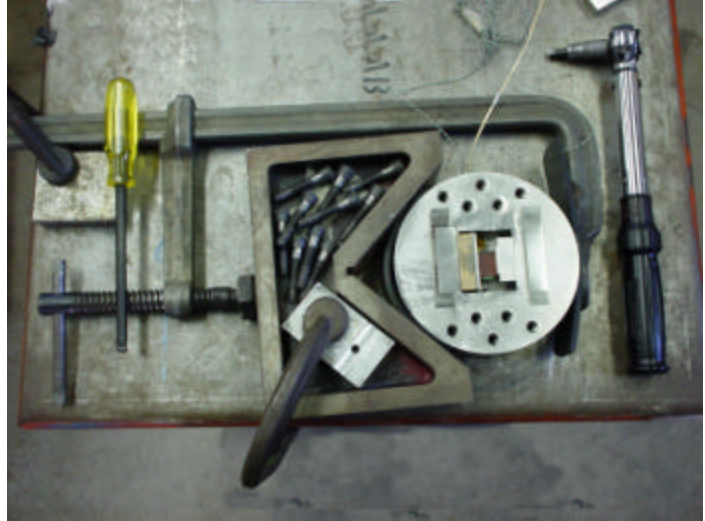


**Figure 9** Top view of preparation fixture for bi-axial measurement. The test fixture is clamped (with rubber grips) inside a triangular frame to disable movement from bolting torque, which also provides a nice holder for the bolts during preparation.

Stainless steel shims, varying in thickness between 0.020 in, 0.005 in, and 0.003 in, are stacked atop the fixture base, on both sides of the test bed (see Figure 9), to the level of shimming required for the desired vertical stress. Vertical stress within the fixture is determined by the distance the upper wedge is driven by the fixture top into the test bed, which is regulated by the amount of shimming placed between the fixture base and top. The relation between vertical stress  $\sigma$  (in MPa) and shimming  $s$  (in inches),

$$s = -2376.6s + 188.91, \quad E = E_{epoxy}$$

$$s = -7589.3s + 534.88, \quad E = E_{G10}$$

$$s = -8324.1s + 663.18, \quad E = E_{aluminum}$$

was established in a calibration of the fixture's wedge mechanism detailed in Appendix 4. The fixture top is then carefully lain upon the shims so as not to disturb their alignment.

A set procedure is required when bolting the top to the base during preparation of the bi-axial test fixture. The bolts are tightened in a spiraling zig-zag order, so as best to balance pressure on the shims throughout the process. Each bolt is tightened with a torque wrench to an approximate torque of 200 in-lbs. For achieving uniform pressures within the fixture, it is critical that the top plate, when bolted, sit parallel to the base. This parallelism is determined after the initial tightening of the four corner bolts; it is therefore necessary to adjust the balance between these four bolts

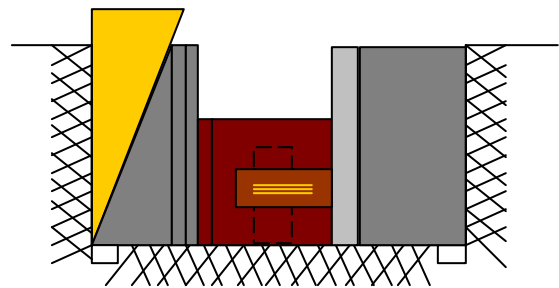


**Figure 10** Cross section of bi-axial test components in test fixture, including (left-right), beryllium copper wedge, steel wedge, two steel shims, capacitance gauge, test sample (instrumented with strain gauges in cross-wise configuration), and steel ram (with short surface against sample).

during this initial tightening phase, by alternately tightening and loosening each corner while visually monitoring the gap between the plates about the whole circumference of the fixture, until the plates are satisfactorily parallel. Since the wedge side of the fixture gives more resistance to the downward force of the top plate, the corner bolts on this side of the fixture are best tightened first, followed by the two corner bolts on the other side of the fixture. Once the corner bolts are tightened, with plates parallel, the remaining bolts are tightened to the desired torque. Because the first bolts are partially relieved of their loads as more bolts are tightened, 2-3 bolting cycles may be required to tighten all ten bolts at the desired torque; however, the bolts must not be torqued beyond the point indicated by the click of the torque wrench, lest they fracture.

Once sealed, the test fixture is removed from the preparation fixture and placed inside the load cell as before, with the ram sitting atop the sample and the wires led through the load cell base.<sup>9</sup> Finally, the base is sealed to the load cell cylinder, the strain gauge wires are connected to their circuit, and the capacitance gauge cable is plugged into a separate circuit on the other side of the load cell cylinder.

*Measurement:* The circuit, which passes through a channel scanner and an LCR meter, is monitored by the same Labview program as before. The measurement proceeds in the same way as the uni-axial loading test, in both sample orientations. The measurement is repeated for several different vertical stresses between 0 MPa and 100 MPa.

### III. Data and Results

*Data Analysis:* The vertical pre-stress applied to the sample by the test fixture is measured and calculated according to the method outlined in the discussion of the fixture vertical stress calibration in Appendix 4. This method involves, in particular, measuring a series of zero-load capacitance and resistance values, using a special addition to the software described in the appendix, as well as a similar series of values following pressurization of the fixture. By taking the difference of these values, stress is calculated according to the capacitance gauge calibration, as well as by extension from a strain calculation derived from the resistance values by the usual method. These strain values obtained from the strain gauges are plotted against the stress read by the capacitance gauge in order to check that the sample is loaded symmetrically in the vertical direction, before proceeding to horizontal loading. Data from horizontal loading by the piston is analyzed as before and plotted against expected values predicted for both free loading and constrained loading. Both the constrained modulus is calculated from the data in the same fashion as in the uni-axial measurement, and the free modulus is derived from that value according to the experimental model. No Poisson ratio is calculated, since this ratio between axial and lateral strain does not hold as one approaches the infinitely rigid constraint condition; however, the magnitude of the Poisson strain is a helpful indicator for gauging the real  $f$ -factor correction which indexes the extent to which the vertical pre-stress approximates the infinitely rigid constraint.

*Results:* Though the loading measurements were relatively straightforward following the extensive debugging of the vertical stress mechanism detailed in Appendix 4, there appeared during the course of the measurements a new, unavoidable asymmetry in the vertical stress on the sample, as indicated by the initial strain gauge check following pre-stress, which introduced significant uncertainty in the mechanical dynamics during bi-axial loading. A pre-stress measurement study, detailed in Appendix 5, demonstrated this asymmetry to be independent of the orientation of the sample, capacitance gauge, or any of the other bi-axial elements, but rather was fixed by the orientation of the fixture; repeated measurements showed strain gauges located on one side of the fixture—the side with the gauge-lead groove—registered highly excessive strains while gauges on the other side registered little or no strain. A precision precise quality check of the fixture's dimensions confirmed the problem, revealing a non-trivial deviation of  $0.0030 \pm 0.0005$  inches from parallelism between the walls of the fixture test bed involved in

---

<sup>9</sup> Note: Care must be taken to assure that the two large shims placed inside the fixture between the capacitance gauge and the lower wedge, do not interfere with the edges of the steel ram, which is a possibility in a situation of extreme deformation of a soft sample under a large vertical load.

the chain of vertical stress—a sure cause of stress concentration. The probable cause of this deviation was plastic deformation of the fixture walls during an accidental stress concentration at very high pressures, which were likely attained during the less precise, initial stages of the fixture calibration; pressures greater than 200 MPa were generated inside the fixture (and on one occasion, left pressurized overnight in this condition, because friction between the wedges prevented the stress mechanism from returning to equilibrium), so that any stress concentration would have exceeded stainless steel’s relatively low plastic threshold. Though the problem could not be entirely eliminated, the study showed that orienting a softer test sample (this result was less successful with the aluminum sample) in the test bed with a particular orientation of the strain gauges resulted in a slightly under-measuring, but symmetric loading result, as indicated by the initial strain gauge check following vertical pre-stress. In this arrangement, the sample was oriented so that the vertical strain gauge, responsible for registering the axial stress from the vertical stress mechanism, was positioned on the under-measuring side of the fixture; we label this the “CG = FUMS” condition (i.e., compressive gauge = fixture under-measuring side). Though the fixture deviation’s precise effect upon the mechanics of the bi-axial loading are not well understood, the achievement of symmetric vertical pre-stress combined with bi-axial loading data in acceptable compliance with theoretical expectations gave us reasonable confidence in the results of the bi-axial measurements.

Our best results for warm bi-axial loading are displayed in Figure 11.

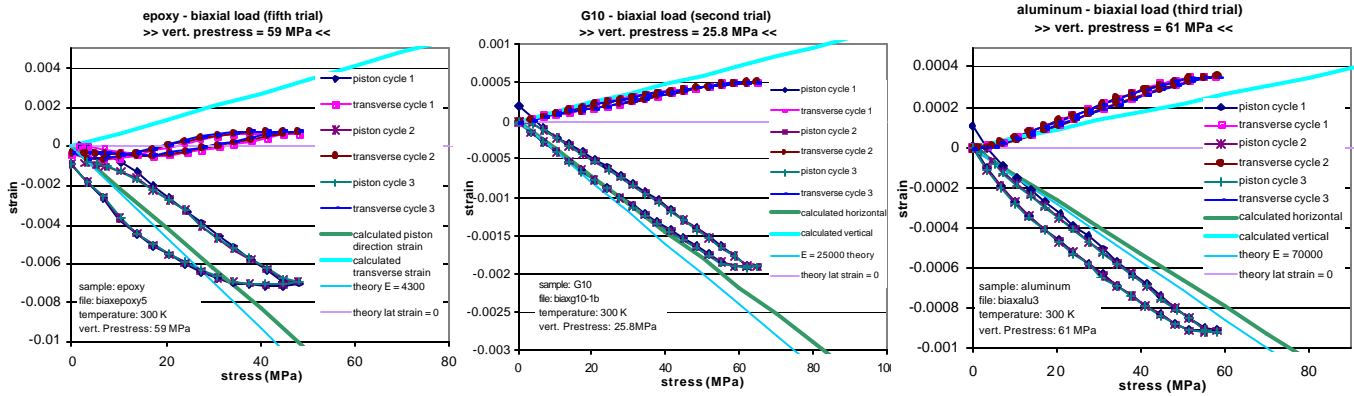


**Figure 11** Best results warm bi-axial loading of epoxy, G10, and aluminum samples. The change in Poisson behavior with increasing modulus demonstrates the expected shift from the constrained loading case to the free loading case discussed in the experimental model.

The  $E$  values calculated directly from our measurement data, that is, the measured constrained moduli—for the epoxy, G10, and aluminum samples—are plotted against the accepted values for the free modulus in Figure 12. In addition, all of the calculated  $E_{constrained}$  and  $E_{free}$  values are compiled in Table 3 of Appendix 3. The systematic statistical error for this measurement increased less rapidly with modulus than the previous measurements, by the relation

$$|\Delta E(stat.)| = 1771.4 \ln(E) - 15791 \quad (14)$$

though there was additionally, in this measurement, a systematic negative deviation from the expected constrained modulus values, which required a positive correction to measured values which increased exponentially with constrained modulus

$$\Delta E_{constrained}(syst.) = +175.59e^{0.000006E_{constrained}} \quad (15)$$

as can be seen clearly in the deviation of measured values from the theory line plotted in Figure 13. This systematic correction is physically plausible, since the vertical constraint effect diminishes sharply as the sample modulus approaches fixture modulus. The dramatic increase, indeed apparent “over-compensation”, of the real  $f$ -factor in our measurements, with increasing modulus, can readily be seen by comparison of the Poisson strains exhibited in the measurements in Figure 11.

Our final mean measured values for  $E_{\text{constrained}}$  and  $E_{\text{free}}$  in warm bi-axial loading were in good compliance with the accepted values. The mean measured value of  $E_{\text{epoxy\_constrained}} = 5,246.34 \pm 730.37(\text{stat.}) + 181.21(\text{syst.})$  MPa and of  $E_{\text{epoxy\_free}} = 4,686.71 \pm 652.46(\text{stat.}) + 180.60(\text{syst.})$  MPa, which have a 8.99% deviation from the accepted values of 4,813.45 MPa and 4,300 MPa respectively; the mean measured value of  $E_{\text{G10\_constrained}} = 29,302 \pm 1,934.98(\text{stat.}) + 209.34(\text{syst.})$  MPa and of  $E_{\text{G10\_free}} = 26,491.26 \pm 1,749.34(\text{stat.}) + 205.84(\text{syst.})$  MPa, which have a 5.97% deviation from the accepted values of 27,653 MPa and 70,000 MPa respectively; and the mean measured value of  $E_{\text{aluminum\_constrained}} = 60,973.72 \pm 5211.67(\text{stat.}) + 253.15(\text{syst.})$  MPa and of  $E_{\text{aluminum\_free}} = 56,547.03 \pm 4,833.30(\text{stat.}) + 246.52(\text{syst.})$  MPa, which have a 19.22% deviation from the accepted values of 75,480 MPa and 70,000 MPa respectively.

## B. Cold Measurement

### I. Experimental Model

In general, the cold bi-axial loading test combines aspects of the cold uni-axial test and the warm bi-axial test. The intersection of the possible samples for these measurements meant that only the G10 sample was subjected to this test, since the epoxy sample could not endure cooling to 4.2 K and the aluminum sample, because of its stiffness, proved problematic for the bi-axial measurement (see Appendix 5). No integrated thermal contraction was measured in this test, since the sample was strained before cooling, preventing a clean measurement of that quantity.  $E$  and  $\nu$  were measured by the conventional method, as a function of measured stress and strain. For this test, the expected modulus was determined according to the model presented in the discussion of the warm bi-axial loading test (Equation 12), applied in this case to the free modulus of the sample at 4.2 K. Applying the theory, then, to the cold free modulus of G10,  $E_{\text{G10\_free}} = 31,250$  MPa, and noting that the  $f$  factor correction involves here the ratio of the *cold* sample and fixture moduli (see Table 1), we expected a cold constrained modulus for G10 of  $E_{\text{G10\_constrained}} = 34,484$  MPa.

Vertical pre-stress was applied to the sample by the same mechanism as in the warm bi-axial load test, with the sample oriented in the CG = FUMS orientation so as to avoid a distorting asymmetric load caused by the fixture deviation. Pre-stress was selected according to the fixture calibration which was employed in the warm bi-axial load test (see Appendix 4), using for G10 the relation

$$\mathbf{s} = -7589.3s + 534.88, \quad E = E_{\text{G10}}$$

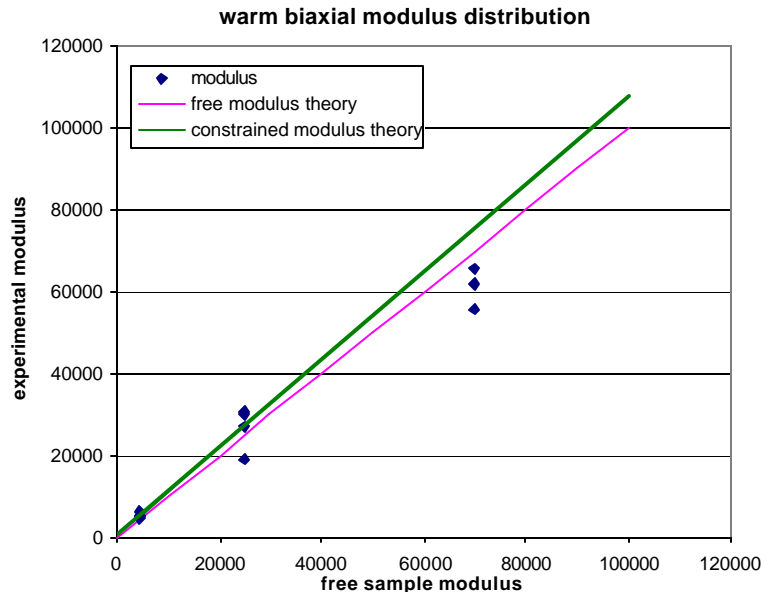


**Figure 12** Plot of modulus values for good warm bi-axial loading tests on epoxy, G10, and aluminum samples vs. accepted free modulus values. Though the modulus values plotted represent constrained loading moduli, the free modulus theory line is displayed alongside the constrained modulus theory line.

where  $\sigma$  is the vertical stress in MPa and  $s$  is the shimming in inches, to determine the desired vertical pre-stress at room temperature.

The cold bi-axial load test presented a significant new problem, however, with the change in the fixture's vertical pre-stress following cool-down from room temperature to 4.2 K due to the combined effects of differential integrated thermal contraction of the elements involved in the stress mechanism, as well as varying relative increases in their mechanical moduli over the same temperature range. Understanding this process was critical to determining the appropriate vertical pre-stress at room temperature, since the measurement was to be performed at 4.2 K, and it was therefore only the pre-stress remaining following cool-down which was of practical use for providing the desired constraint effect upon the sample during horizontal loading. Indeed, determining this outcome precisely was of decisive importance in the case of the measurement's ultimate test objective, the cable ten-stack, since any near-total loss of the vertical support stress during cool-down would place the sample in the precarious mechanical situation of free uni-axial loading, in which it risked certain mechanical failure. The precise relative contributions of the thermal and mechanical factors in the change of the fixture's vertical pre-stress following cool-down to 4.2 K were computed in a model which is detailed in Appendix 6. The result demonstrates the peculiar precision required for the choice of pre-stress at room temperature, since not only the magnitude, but also the direction, of vertical pre-stress change depends both on the integrated thermal contraction of the test sample *and* on the magnitude of vertical pre-stress applied at room temperature (see Figures 47 in Appendix 6). In the model, differential thermal contractions may either reduce or augment pre-stress, depending upon whether the differential thermal contraction between the sample and the fixture is positive or negative, while the increase in moduli of non-steel fixture elements following cooling always contributes to an increase. In the case of the G10 sample, whose thermal contraction is less than that of the stainless steel fixture (see Table 2), the change in vertical pre-stress following cool-down is positive only, regardless of warm pre-stress, according to the relation

$$\Delta \mathbf{s}_{\Delta T} [E_{G10}(T), \mathbf{e}_{\Delta T G10}] = 0.1853 \mathbf{s}_{warm} + 1.3307 \text{ MPa} \quad (16)$$

since the only potentially negative factor in the pre-stress change—the differential thermal contraction between the sample and the fixture—contributes positively rather than negatively: with the sample contracting less than the fixture, the fixture effectively tightens around the sample, thereby increasing the compressive stress. (On the contrary, in the ultimately more interesting case of the cable ten-stack, whose integrated thermal contraction—approximately 4.45 mm/m—is greater than that of the fixture, the direction of pre-stress change is dependent upon the magnitude of vertical pre-stress at room temperature; the magnitude of warm pre-stress selected for the cable is therefore highly sensitive for the success of the measurement.)

The vertical stress was measured with the capacitance gauge as before, using the same gauge calibration for measuring vertical stress at room temperature, and using a different gauge calibration when measuring vertical stress at 4.2 K, given by

$$C = 0.0002651 \mathbf{s} + C_0 \quad (\text{CC10SC1})$$

$$C = 0.0002674 \mathbf{s} + C_0 \quad (\text{CC10SC2})$$

where  $C$  is again the capacitance value in nF and  $\sigma$  the pressure in MPa. The vertical stress in the fixture following cool-down to 4.2 K could thus be calculated with measurements from the capacitance gauge, though, since it was not possible during the course of this measurement to obtain  $C_0$ , the zero-load capacitance value at 4.2 K, the  $C_0$  value obtained at 4.2 K during the cold uni-axial loading test (see cold uni-axial preparation procedure) was substituted in its place. The same substitution was made for the zero-load strain gauge resistance value, required for calculating the vertical stress by extension from the vertical strain registered by the vertical strain gauge.

Horizontal stress was applied directly by the load cell piston as before. Vertical and horizontal strain were likewise measured in the same way as before, with resistive strain gauges affixed to the test sample in cross configuration.

## II. Measurement Apparatus and Procedure

*Preparation:* The procedure for the cold bi-axial loading test combines aspects of the cold uni-axial loading test and the warm bi-axial loading test. The fixture is first prepared with a vertical pre-stress at room temperature according to the procedure of the warm bi-axial loading test (assuring, among other things, the CG = FUMS sample orientation), taking care, however, to select a pre-stress which is permissible for the cold bi-axial measurement, as determined by the model for change of pre-stress due to cooling, presented in the above discussion of the experimental model. While the system is prepared for cool-down, by the same procedure as for the cold uni-axial loading test, a pre-cooling warm bi-axial load test is performed to determine the shape of the data before cool-down; the entire assembly is then cooled by liquid helium transfer according to the same procedure outlined before. Once the system is cooled to 4.2 K and the fixture is submerged in liquid helium, a series of non-loading capacitance and resistance measurements are made, by the same procedure as in the zero-load measurements made at 4.2 K for the cold uni-axial loading test; combining these cold pressurized values with the cold zero-load values obtained during the cold uni-axial measurement, the fixture's cold vertical pre-stress may be calculated approximately, in order to verify the prediction that sufficient vertical pre-stress would remain following cool-down to confine the sample during horizontal loading. Assuming this is the case, the bi-axial loading test may proceed. Liquid helium transfer is terminated once the liquid has reached a level sufficient for the intended set of measurements.

*Measurement:* The measurement procedure is identical to that of the cold uni-axial loading test.

*Disassembly:* Once the intended set of measurements is completed, the system is disassembled according to the procedure outlined for the cold uni-axial loading test.

## III. Data and Results

*Data Analysis:* Data analysis for the cold bi-axial loading test is the same as for the warm bi-axial loading test in almost every respect, replacing warm values with the equivalent cold values where appropriate. Cold vertical pre-stress is calculated and analyzed by the same method as for warm vertical pre-stress, with the exception that the zero-load capacitance and resistance values are provided by a prior measurement (the cold uni-axial loading test) because of the practical constraints imposed by cooling with liquid helium. Performing a cold vertical stress asymmetry check, like the warm check, by plotting cold sample strains against the capacitance gauge cold vertical pre-stress, is a useful exercise, but it is fundamentally imprecise because of the intrinsic problems with the method by which the values are calculated. Data from horizontal loading by the piston is analyzed in the same fashion as in the warm bi-axial loading test.

*Results:* The cold bi-axial loading test, reached at the end of the calibration program, was short-changed because of time constraints. As a result, only one measurement was performed. Unfortunately, in addition, the measurement was a poor one, both in terms of execution—problems were encountered with piston loading which distorted results—and in terms of results—the data did not conform well to expected values. The key points of data analysis for this measurement are displayed in Figures 13 and 14. The measurement yielded a cold constrained modulus of  $E_{G10\_constrained} = 58,311.88$  MPa and a cold free modulus of  $E_{G10\_free} = 52,843.68$  MPa, which have a 69.09%

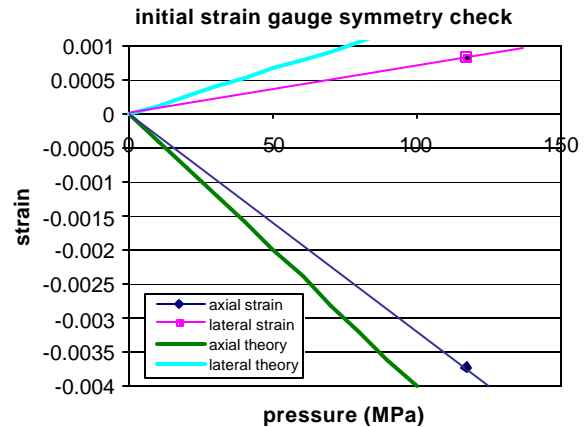


**Figure 13** The pre-cooling vertical pre-stress symmetry check for the only cold bi-axial load test on the G10 sample, with the sample in CG = FUMS orientation, shows the characteristic loading of this condition: slightly under-measuring but symmetric strains.

deviation from the expected values of 34,484 MPa and 31,250 MPa respectively.

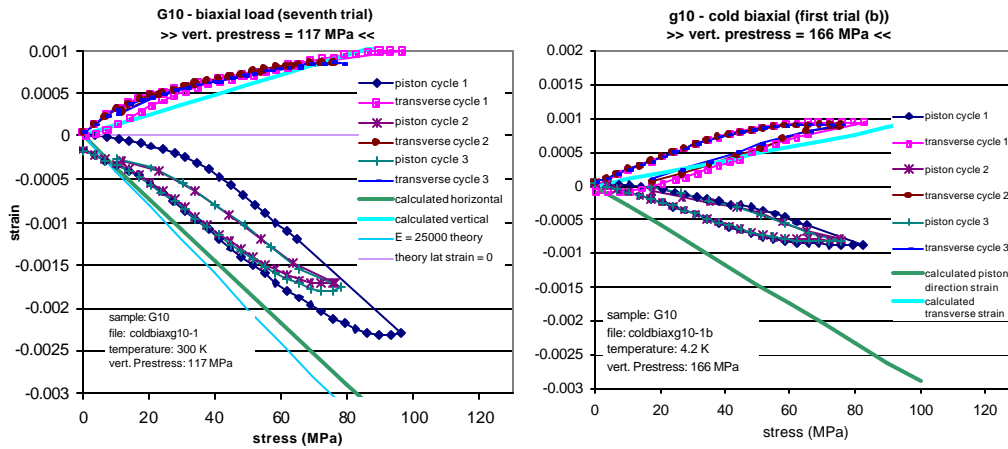


**Figure 14** Pre-cooling warm bi-axial loading test, with a vertical pre-stress of 117 MPa, and final cold bi-axial loading test, with vertical pre-stress increased to 166 MPa (as read by the capacitance gauge) following cool-down, for the only cold bi-axial loading measurement on the G10 sample. Measurements results were poor primarily because of uncontrolled piston loading by the load cell.

Despite the disappointing results, the test was a useful exercise in testing the predictive model for the change in pre-stress due to cooling. Measurements yielded a pre-stress change from a warm vertical pre-stress  $\sigma_{[T=300\text{ K}]} = 117\text{ MPa}$  to a cold vertical pre-stress of  $\sigma_{[T=4.2\text{ K}]} = 166\text{ MPa}$ , a  $\Delta\sigma_{\Delta T} = +49\text{ MPa}$ , which was different from the predicted value of  $\Delta\sigma_{\Delta T} = +23.0\text{ MPa}$  by 112.9%.

### CONCLUSION

The calibration of the bi-axial loading fixture was largely successful, producing measurements of Young’s modulus ( $E$ ), the Poisson ratio ( $\nu$ ), and the integrated thermal contraction from  $T = 300\text{ K}$  to  $T = 4.2\text{ K}$  ( $\epsilon_{\Delta T}$ ) for epoxy, G10, and aluminum test samples, which were generally in reasonable compliance with accepted values and their associated theories. The mean values, and associated errors, for the key measured values in each test are listed in Tables 4 and 5. Deviations ranged generally 0-20% from

<i>Test: Uni-axial Warm</i>						
<i>sample</i>	<i>E<sub>avg</sub> (MPa)</i>	<i>st. dev.</i>	<i>deviation</i>	<i>n<sub>avg</sub></i>	<i>st. dev.</i>	<i>deviation</i>
epoxy	4216.84	336.75	0.0193	0.477	0.116	0.4442
G10	23758.15	2312.33	0.0497	0.348	0.179	0.0539
aluminum	70764.20	8120.77	0.0109	0.346	0.075	0.0491
<i>Test: Uni-axial Cold</i>						
<i>sample</i>	<i>E<sub>avg</sub> (MPa)</i>	<i>st. dev.</i>	<i>deviation</i>	<i>n<sub>avg</sub></i>	<i>st. dev.</i>	<i>deviation</i>
G10	38167.51	996.37	0.2214	0.607	0.000	0.8384
aluminum	76874.64	12994.73	0.0956	0.317	0.075	0.0400
<i>Test: Bi-axial Warm</i>						
<i>sample</i>	<i>E<sub>constrained avg</sub> (MPa)</i>	<i>st. dev.</i>	<i>deviation</i>	<i>E<sub>free avg</sub> (MPa)</i>	<i>st. dev.</i>	<i>deviation</i>
epoxy	5246.34	730.37	0.0899	4686.71	652.46	0.0899
G10	29302.40	1934.98	0.0597	26491.26	1749.34	0.0597
aluminum	60973.72	5211.67	0.1922	56547.03	4833.30	0.1922

**Table 4** Summary of mean values for mechanical properties of the calibration samples measured in each of the statistically significant loading tests.

<i>Test: Integrated Thermal Contraction (Uni-axial Cold Data)</i>			
sample	$\epsilon_{T_{avg}}$ (mm/m)	st. dev.	deviation
G10	2.40	0.84	0.1198
aluminum	5.21	0.11	0.1843

**Table 5** Summary of mean values for the integrated thermal contraction of the G10 and aluminum samples, as measured during the course of the cold uni-axial loading test.

accepted values, which is an acceptable range, considering the imperfect measurement apparatus available for the measurements (load-cell hydraulics, in particular, were a persistent problem which threatened to distort measurement data with irregular loading rates). Throughout the calibration process, accuracy and consistency of measurements was improved through improved understanding of the measurement system.

At the limit of improvement to the measurements, systematic modulus-dependent errors of the measurements, both of a random (i.e. statistical) and particular nature, were specified in order to define the certainty of our measured values. Random errors were specified in Equations 5, 6 and 14, and are plotted together in the first graph of Figure 15; a particular systematic deviation in the modulus values measured in the warm bi-axial measurement was also characterized in Equation 15, and is plotted versus constrained modulus in the second graph of Figure 15.

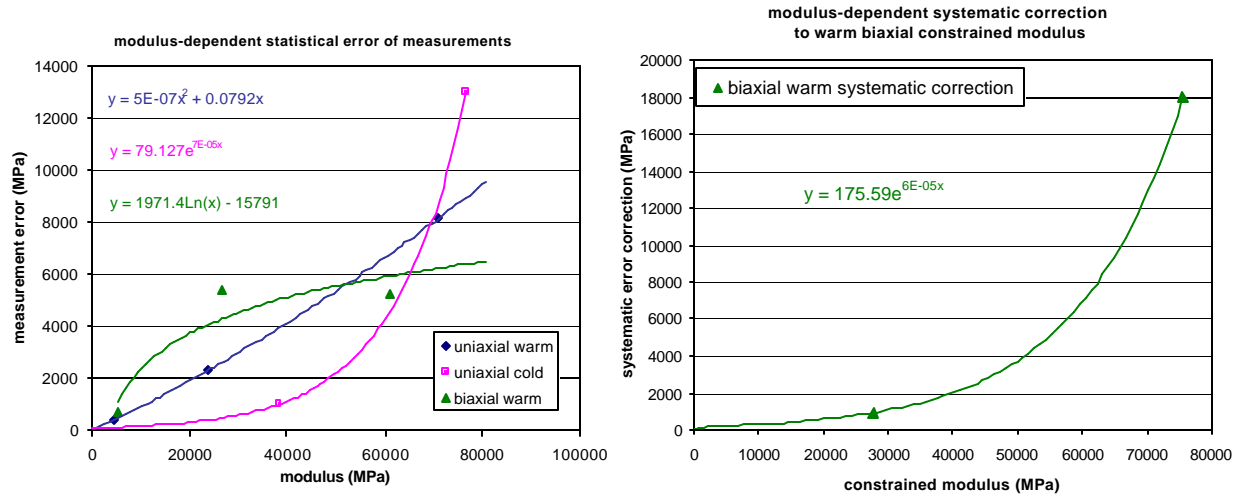
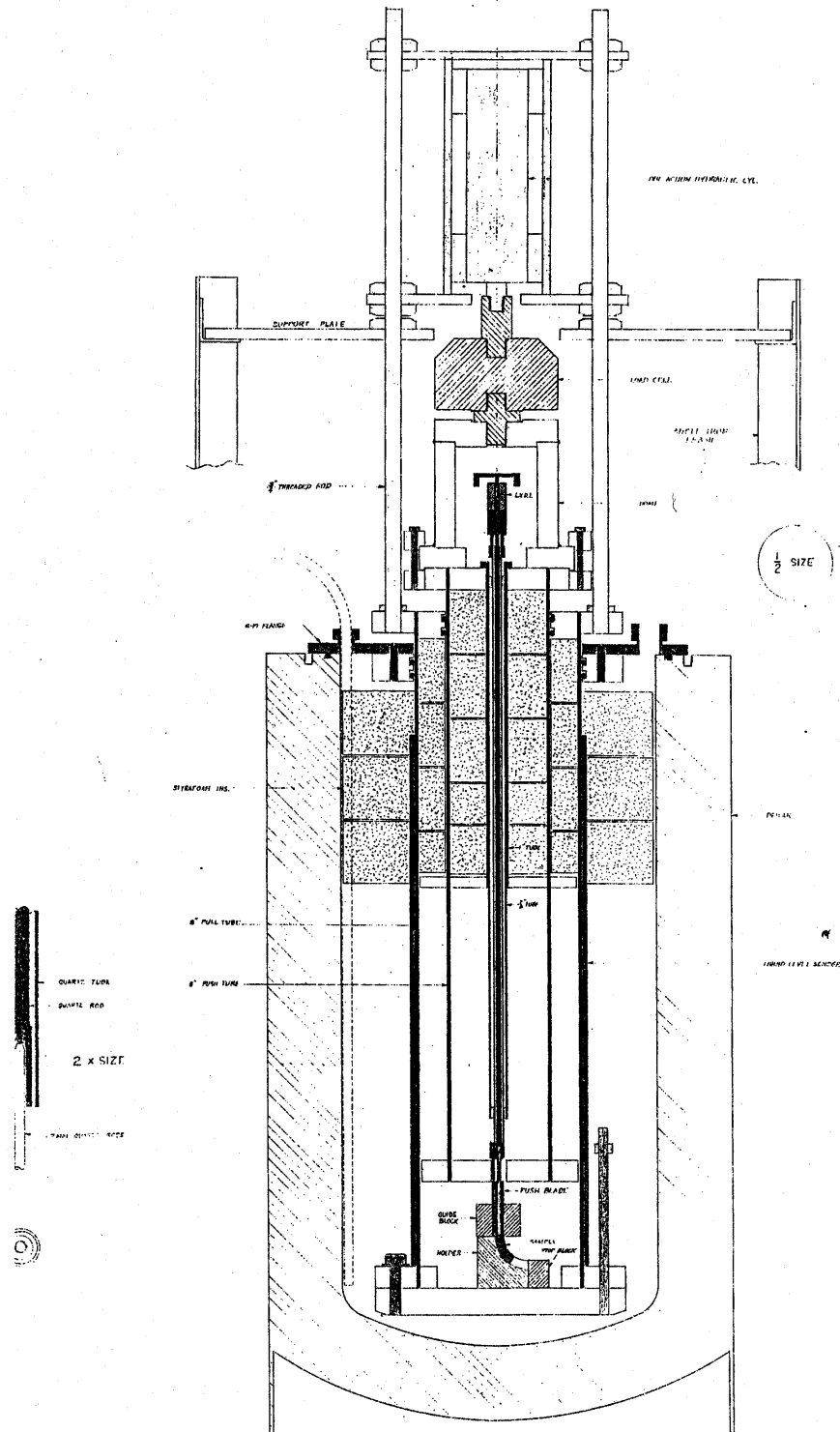


**Figure 15** Systematic modulus-dependent statistical errors, specified by Equations 5, 6 and 14, for the warm uni-axial, cold uni-axial, and warm bi-axial measurements, respectively, are plotted in the first graph. In addition, the systematic correction required for the warm bi-axial measurement, specified by Equation 15, is plotted in the second graph.

Finally, some problems, or errors, in the measurements were found to be ultimately inescapable with the existing measurement apparatus. Among these problems, the fixture deviation and irregular piston loading figured prominently. Nevertheless, good measurements remained achievable, since these problems were well understood, and data which was affected by their distortions was either discarded or corrected by means of analysis techniques, like the derivative plots displayed in Appendix 2. The extensive understanding of the measurements achieved during the calibration bolsters confidence in future measurements of the thermo-mechanical properties of real cable ten-stacks.

# Appendix 1

## Experimental Apparatus: Load-Cell



## Appendix 2

### Peculiarities and Pitfalls of Warm Uni-axial Loading

Deviations in the warm uni-axial load test data from the expected linear result were analyzed and modeled on a basis of observations concerning a variety of soft components in the measurement system.

The chief cause of error throughout initial experimental trials was the presence of a fluid glue layer in the chain of loading, placed underneath the test sample in order to fix its position on the fixture base. Under stress, this initially uniform soft layer dispersed beneath the sample, magnifying any perturbations from uniform loading along the sample surface. Figure 1 illustrates an extreme of such settling during successive loading cycles on the aluminum sample; this particular case represents a settling of the hysteresis behavior of the elastic glue bond between the sample and the strain gauge, a phenomenon which is modeled in Figure 6. Figures 2 and 3 show a different settling effect, between successive loading cycles, caused by a soft adhesive layer beneath the sample provided to fix the samples

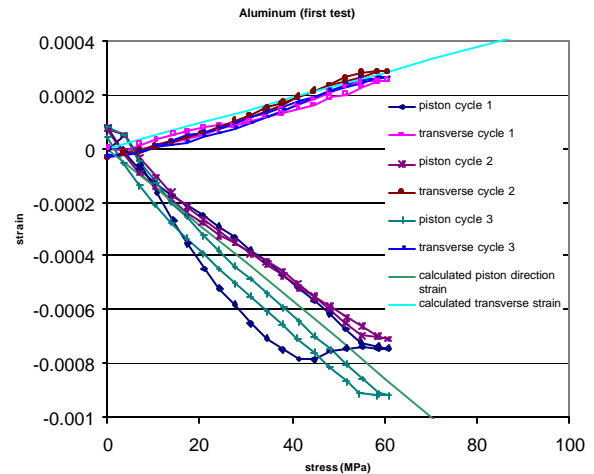


**Figure 1** Significant hysteresis settling displayed in first run of warm uni-axial calibration of aluminum sample. (filename: al1)

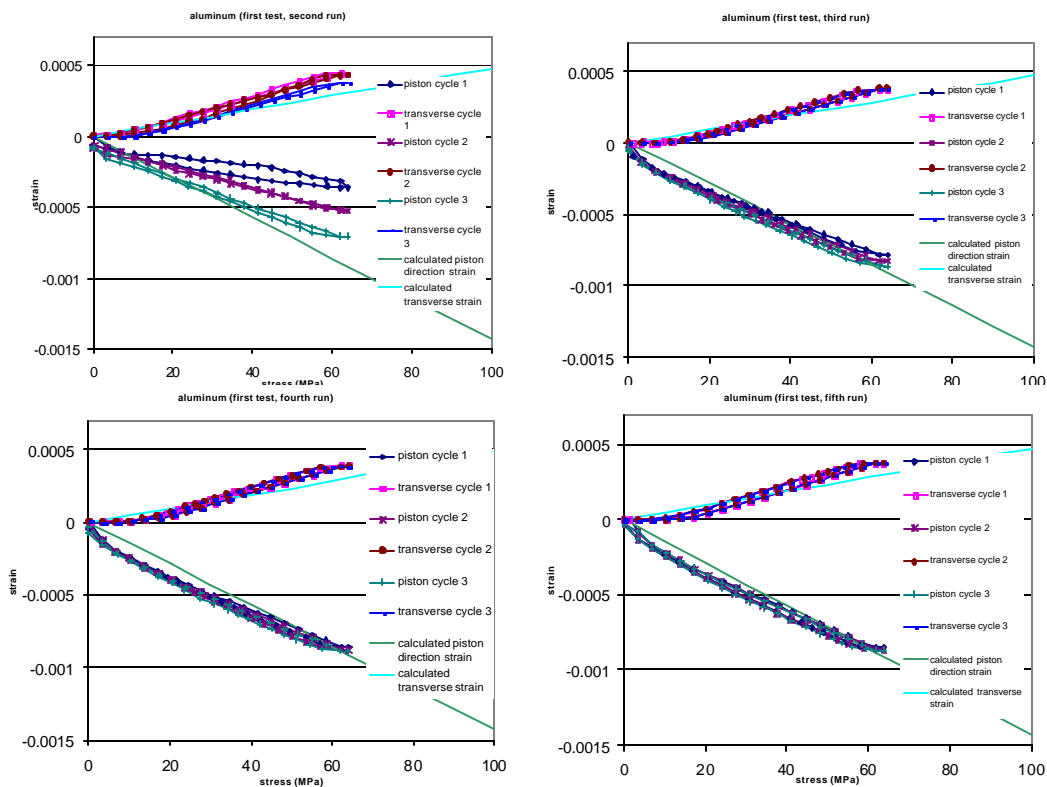


**Figure 2** First test, second through fourth runs of warm uni-axial calibration of aluminum sample, showing repeated loading regularizing the data between loading cycles. This effect is caused by significant softness in the system which plastically transforms with each loading. (filenames: alrun3-1 - alrun3-4)

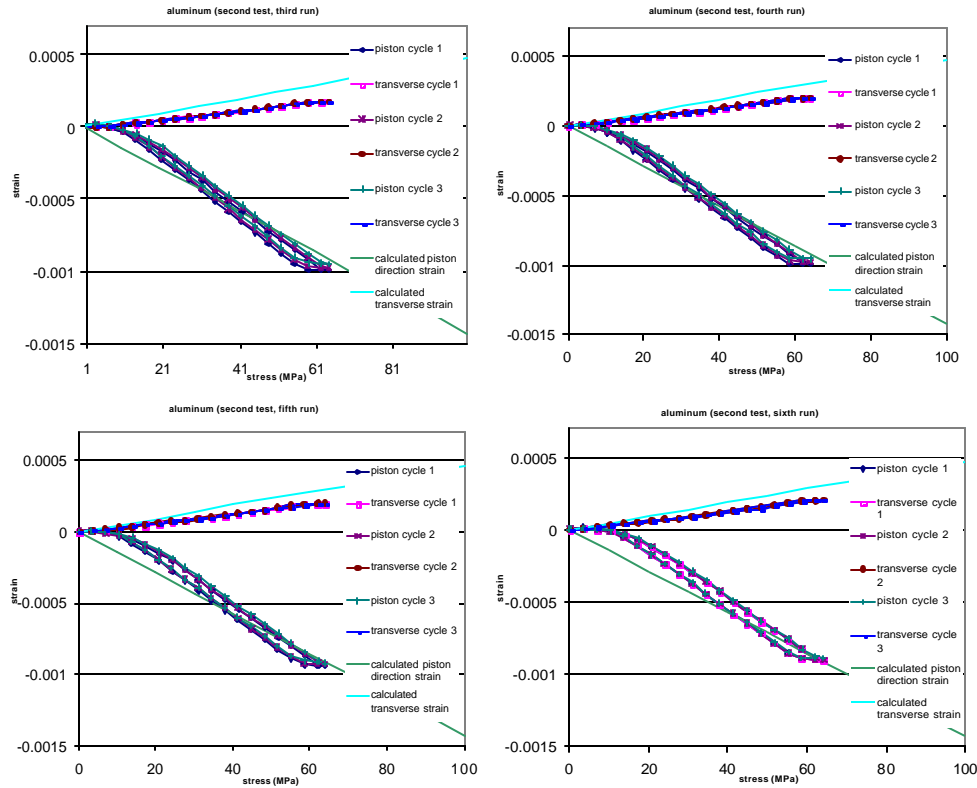


**Figure 3** Second test, third through sixth runs of warm uni-axial calibration of aluminum sample, showing same effect as in Fig. 2. (filenames: alrun3-6 - alrun3-9) lateral position in the fixture (the effect is less pronounced in Figure 3 than in Figure 2).

The inhomogeneous distribution of the resulting dispersed glue beneath the sample introduced dramatic uncertainties into our measurements of  $E$  and  $\nu$ . Initial measurements for aluminum and stainless steel test samples produced values with ranges of  $50359 \text{ MPa} < E_{\text{aluminum}} < 84731 \text{ MPa}$  (an error of  $\pm 25\%$ ) and  $127361 \text{ MPa} < E_{\text{stainless steel}} < 276335 \text{ MPa}$  (an error of  $\pm 50\%$ ). A pattern in this error was readily evident and came to be labeled “fork rotation”, or data asymmetry. This behavior is displayed for our aluminum and stainless steel tests in Figure 4. The first attempt at rectifying this error, by recutting the test samples

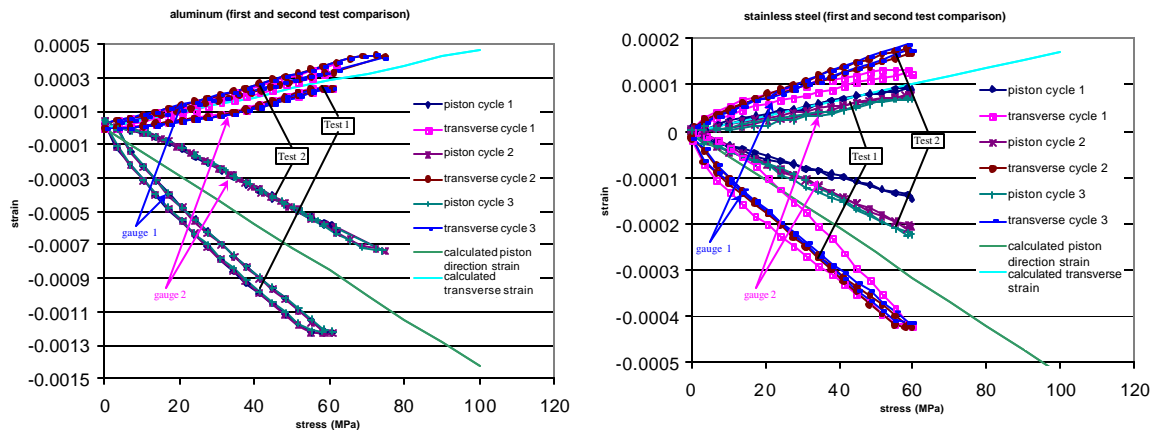


**Figure 4** Strain data from our first complete set of measurements for the warm uni-axial calibration of the aluminum and stainless steel samples. Data should match the calculated strain values, but is instead shifted in one direction for the first test and shifted in the other direction for the second test. In each measurement, gauge 1 reads excessive strain and gauge 2 reads insufficient strain, relative to expected values. (filenames: al2, al4; steel1, steel2)

to have equal pressurizing surfaces between the two orientations, did not eliminate the error, yielding, in our second round of measurements, clearly evident “fork rotation” and modulus values with ranges of  $44393 \text{ MPa} < E_{\text{aluminum}} < 166631 \text{ MPa}$  (an error of +140%, -36%) and  $144260 \text{ MPa} < E_{\text{stainless steel}} < 171850 \text{ MPa}$  (an error of -25%).

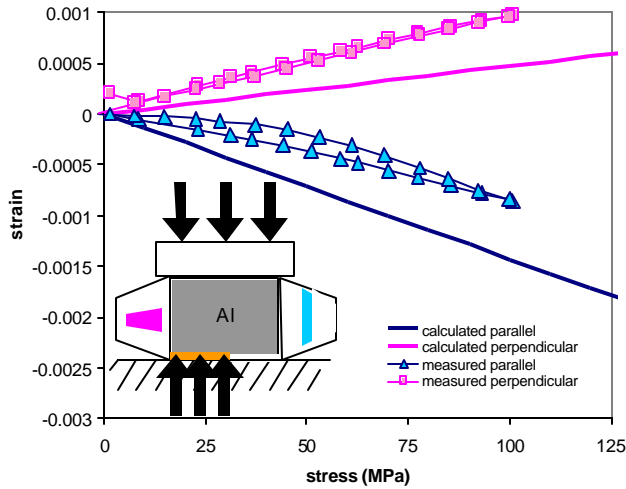


**Figure 5** Model of data asymmetry in uni-axial loading measurements. Inhomogeneous adhesive build-up underneath the sample creates a stress gradient which causes one gauge to register more strain and the other to register less strain than is expected for the given stress applied to the sample.

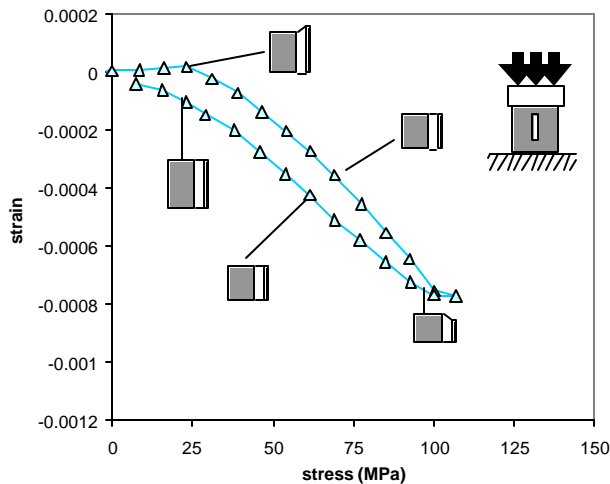


**Figure 6** A model illustrating the cause of hysteresis in the compression-decompression cycle of the gauge, due to the high elasticity of the adhesive bond between the gauge and the sample. Initially, the adhesive stretches while the gauge fails to register the stress applied to the sample. At a certain threshold, the elastic adhesive snaps into phase with the compressed sample, registering a steeper rate of strain/stress increase. The measurement shown was performed on an aluminum sample.

Subsequent observations revealed the glue layer as the source of the “fork rotation.” The “fork rotation” error was discovered to vary between placements of the sample in the fixture test bed. Considering the placement environment within the fixture, we generated a model, illustrated in Figure 5, to account for this dependence. According to the model, inhomogeneous adhesive build-up beneath the sample, caused by stress-induced dispersion of the initially uniform glue layer, creates a stress gradient along the length of the sample. With stress applied unevenly across the sample, the gauge under higher pressure registers a higher strain than expected for the given stress, while the gauge under lower pressure registers a lower strain than expected for the given stress. The model explains why one gauge under-measures in both orientations while the other gauge over-measures in both orientations, and thus why rotation of the data “fork” is observed between tests.

In order to eliminate any such stress gradient, the adhesive tape was removed from the fixture base beneath the sample, the sample surfaces were thoroughly cleaned of residues, and the sample was centered in the test bed with a placement frame made from the sample-impressed tape remaining from prior measurements. This change to the measurement achieved the desired result of significantly eliminating the erroneous data asymmetry and yielding data in acceptable compliance with the expected values predicted by the theory (see discussion of results for warm uni-axial measurement).

Even with this significant error eliminated, other peculiarities in the experimental results remained which must be considered in order to properly analyze the data for calculation of  $E$  and  $\nu$ . A variety of curvatures in the data plots indicated the presence of intrinsic tensile and compressive elasticities in the system. Several specific observations suggested the variable elasticity of the gauge-sample interface was a significant source of the uncertainty. Hysteresis in our data, due to inertial delay in gauge response to sample deformation—made possible by the elasticity of the glue bond between the gauge and the sample (see Figure 6)—presented obstacles to achieving perfect

duplication of the expected results, since data curvature resulting from such effects distorted the linear response expected from a sample under stress.

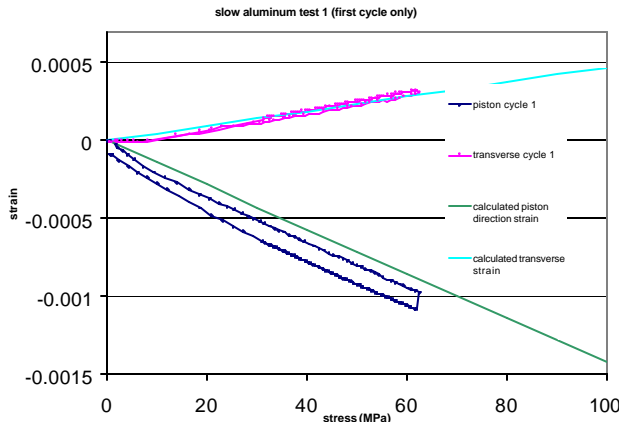


**Figure 7** First slow run of warm uni-axial calibration of aluminum sample, showing constant negative deviation of axial strain values from expected values. (filename: slowal1)

The hysteresis behavior may also be the source of an overcompensation effect in the compressive (axial) gauge in the low-stress region, resulting in a constant negative displacement of values measured by that gauge from the expected values, even when the linear relation was correct. This problem is illustrated in Figure 7. This constant offset of the values, while posing no problem to a calculation of the elastic modulus, would distort calculations of the sample's Poisson ratio. A series of slow stress-ramping tests was conducted, focused in the low-stress region, to examine whether the higher piston ramping rate caused the steep slope in the initial phase of the axial strain gauge data—the source of the constant offset of the higher stress values. This study demonstrated that ramp rate played no role in this behavior (see Figure 8), and that this behavior,

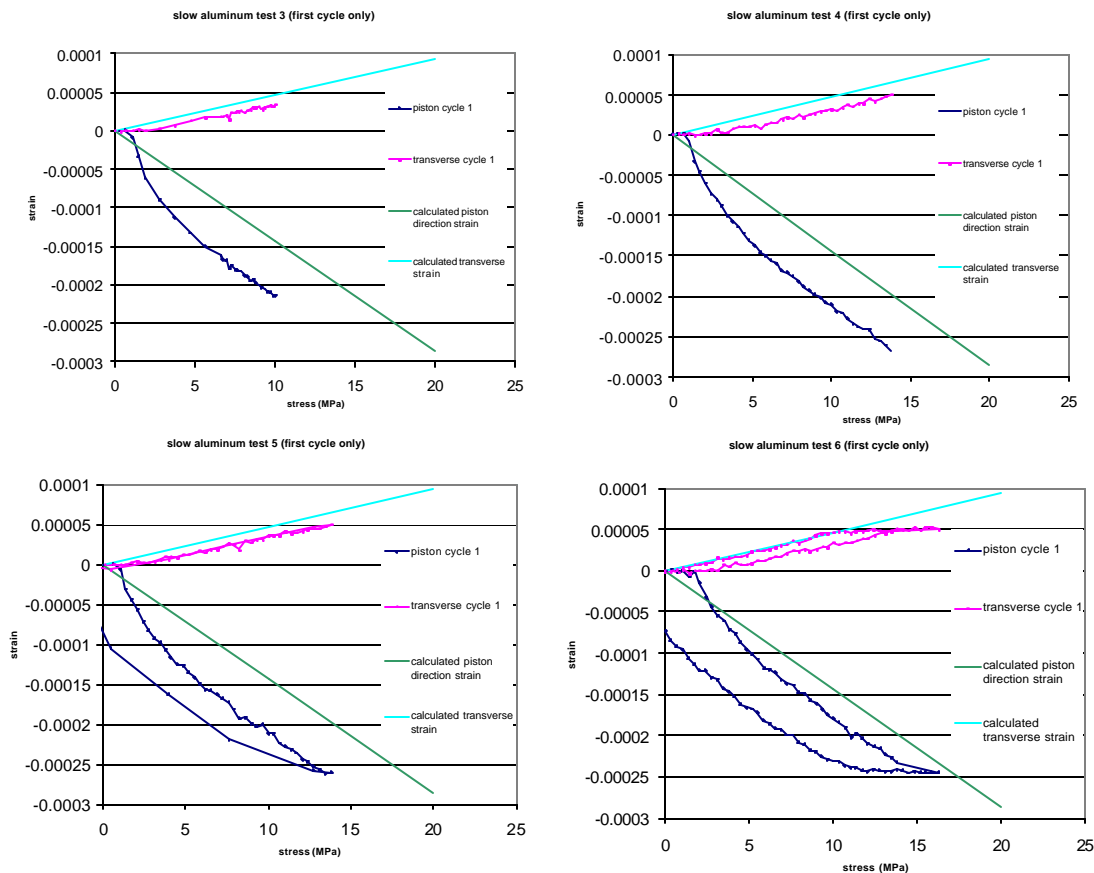


**Figure 8** Third through sixth slow runs of warm uni-axial calibration of aluminum sample, limited to low-stress region. Data exhibits initial delay in gauge response to registered stress ( $\sigma < 1\text{-}3$  MPa), followed by a sharp overcompensating response ( $1\text{-}3$  MPa  $< \sigma < 6\text{-}7$  MPa), before settling into the expected linear response of elastic deformation ( $\sigma > 7$  MPa). (filenames: slowal3 – slowal6)

possibly accounted for by our hysteresis model, was unavoidable with our measurement apparatus.

The likely reason for this unavoidability is that the most highly probable cause of the problem, as it appears in the data, is not the gauge bond hysteresis, but rather a loading delay in the load cell itself. As the hydraulic piston is lowered within the load cell cylinder (see schematic in Appendix 1), friction builds, registering pressure in the load cell before sufficient hydraulic pressure builds to overcome the friction and make contact with the sample; this explains the zero-strain phase of the data in Figure 8, since the load-cell registers sufficient pressure to trigger data acquisition by the measurement program, but no strain is measured since the loading piston has not yet made contact with the sample. The second, steep loading slope region of the data,  $1\text{-}3\text{ MPa} < \sigma < 6\text{-}7\text{ MPa}$  (as registered by the load cell), represents the phase in which the piston makes contact with the sample and instantly strains it to the magnitude corresponding to the non-zero stress accumulated in the system during the friction phase, thereby establishing chain of pressure, between the load cell and the load cell base, in a dynamically changing equilibrium. Once this process is completed, the load cell and the sample are pressurized at the same rate, so that the pressure values in the data represent the true stress on the sample, and the sample strains linearly with pressure, as expected. Regardless of the true cause of the offset in the axial strain data, it remains a consistent feature of the data which is unavoidable. The problem is therefore resolved with an offset correction to the data, easily accomplished by re-zeroing the data at the y-intercept of a fit to the linear region of the axial strain data.

Finally, when in certain cases, an unavoidable initial curvature in the loading data is spread over a larger pressure range, the data can be analyzed through a plot of the derivative  $d\epsilon/d\sigma$  vs. stress in order to determine the pressure at which non-linear behavior ends in the cycle and the expected linear behavior begins. Figure 9 provides an example of this useful tool. Occasionally appearing extended curvatures, such as that displayed in the figure, are not well understood physically. One hypothesis is that such behavior results from an initial slipping of the piston ram over the edges of the sample surface, when the piston makes first contact with the ram. This occurrence was apparently observed following a measurement. Regardless of its cause, the data may be corrected by the same analysis as before, with the aid of the derivative plots. Such correction is critical for accurate calculation of the E and  $\nu$  values.

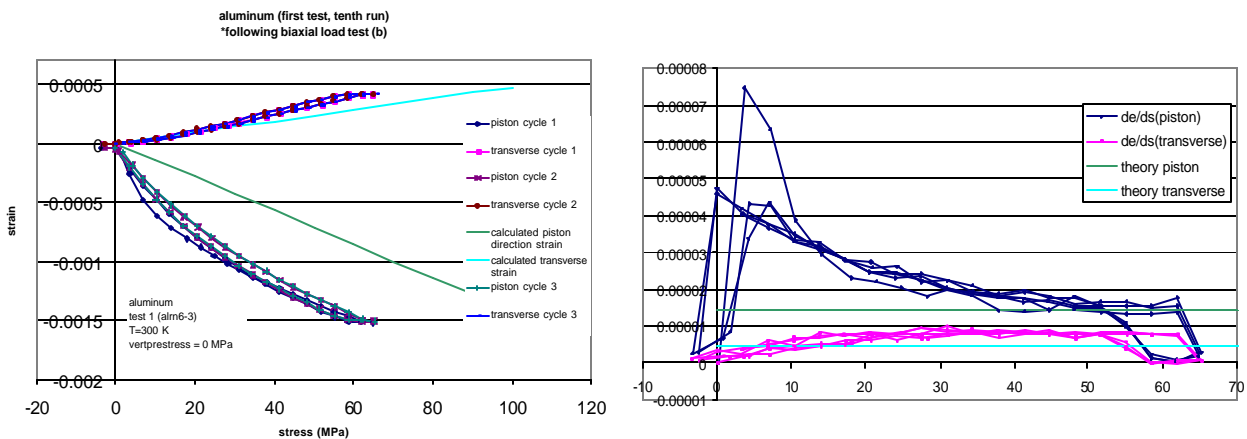


**Figure 9** Comparison of  $\epsilon(\sigma)$  and  $d\epsilon/d\sigma$  plots for purpose of analysis for E and  $\nu$  calculation. While cursory analysis of the  $\epsilon(\sigma)$  plot suggests linear axial strain is achieved in the data for  $\sigma > 20$  MPa, analysis with the  $d\epsilon/d\sigma$  plot shows that a truly linear strain response is present only in the  $45\text{ MPa} < \sigma < 60\text{ MPa}$  range. The lateral (Poisson) strain, on the other hand, is linear in a stress range of  $25\text{ MPa} < \sigma < 60\text{ MPa}$ .

### Appendix 3

#### Tables of Measured Values

<i>Warm Uni-axial Load Test Experimental Values</i>					
<i>trial</i>	<i>filename</i>	<i>E (MPa)</i>	<i>deviation</i>	<b><i>n</i></b>	<i>deviation</i>
<i>Epoxy, <math>E_{theory} = 4,300 MPa</math></i>					
1	epoxy1	4674.28	0.087	0.672	1.035
2	epoxy1-2	4401.09	0.024	0.538	0.629
3	epoxrn2	3663.35	0.148	0.283	0.143
4	epoxrn4-1	4439.51	0.032	0.390	0.181
5	epoxrn4-2b	4476.69	0.041	0.478	0.449
6	newepox1	4042.73	0.060	0.417	0.262
7	newepox4	3923.21	0.088	0.510	0.546
8	newepox6	4113.83	0.043	0.526	0.594
	avg.	4216.84	0.065	0.477	0.480
	st. dev.	336.75		0.116	
<i>G10, <math>E_{theory} = 25,000 MPa</math></i>					
1	g10run1	25092.90	0.004	0.307	0.070
2	g10run3	25908.12	0.036	0.372	0.126
3	g10run4	23283.46	0.069	0.223	0.323
4	g10run5	20900.74	0.164	0.221	0.330
5	g10run6	24310.23	0.028	0.314	0.047
6	g10run7	21400.46	0.144	0.256	0.225
7	g10run8	23554.52	0.058	0.195	0.408
8	g10run9	20967.92	0.161	0.290	0.121
9	coldg10-1	27504.44	0.100	0.646	0.959
10	g10run10	23312.81	0.067	0.699	1.119
11	g10run11	26438.82	0.058	0.261	0.210
	avg.	23879.49	0.081	0.344	0.358
	st. dev.	2230.28		0.170	
<i>Aluminum, <math>E_{theory} = 70,000 MPa</math></i>					
1	alrn5-2b	83525.28	0.193	0.487	0.476
2	alrn5-4	71030.98	0.015	0.295	0.106
3	alrn6-1	72256.61	0.032	0.328	0.007
4	coldalu2	62757.37	0.103	0.274	0.169
5	alrn6-2	73803.07	0.054	0.354	0.072
6	alrn6-3	61211.87	0.126	0.339	0.028
	avg.	70764.20	0.087	0.346	0.143
	st. dev.	8120.77		0.075	

**Table 6** Summary table listing E and  $\nu$  values derived from warm uni-axial load tests of epoxy, G10, and aluminum test samples, with fractional deviation from the accepted values (note:  $\nu_{theory} = 0.33$  in all cases), as well as mean and standard deviation values of the data sets. The E and  $\nu$  values were calculated from the load test data according to the methods described for data analysis in the discussion of the warm uni-axial load test.

<i>Cold Uni-axial Load Test Experimental Values</i>					
<i>trial</i>	<i>filename</i>	<i>E (MPa)</i>	<i>deviation</i>	<i>n</i>	<i>deviation</i>
<i>G10, E<sub>theory</sub> = 31,250 MPa</i>					
1	coldg10-1	38872.05	0.244	0.606	0.838
2	coldg10-2	37462.97	0.199	0.607	0.839
	avg.	38167.51	0.221	0.607	0.838
	st. dev.	996.37		0.000	
<i>Aluminum, E<sub>theory</sub> = 85,000 MPa</i>					
1	coldalu1	91823.96	0.080	0.399	0.208
2	coldalu2	68281.31	0.197	0.251	0.240
3	coldalu2b	70518.66	0.170	0.301	0.088
	avg.	76874.64	0.149	0.317	0.179
	st. dev.	12994.73		0.075	

**Table 7** Summary table listing E and  $\nu$  values derived from cold uni-axial load tests of G10 and aluminum test samples, with fractional deviation from the accepted values (note:  $\nu_{theory} = 0.33$  in all cases), as well as mean and standard deviation values of the data sets. The values were calculated according to the conventional method.

<i>Warm Bi-axial Load Test Experimental Values</i>				
<i>trial</i>	<i>filename</i>	<i>E<sub>constrained</sub> (MPa)</i>	<i>deviation</i>	<i>E<sub>free</sub> (MPa)</i>
<i>Epoxy, E<sub>constrained theory</sub> = 4,813 MPa</i>				
1	biaxepoxy2	5039.04	0.047	4501.52
2	biaxepoxy2b	4625.53	0.039	4132.12
3	biaxepoxy3	5016.56	0.042	4481.44
4	biaxepoxy5	6304.23	0.310	5631.75
	avg.	5246.34	0.109	4686.71
	st. dev.	730.37		652.46
<i>G10, E<sub>constrained theory</sub> = 27,653 MPa</i>				
1	biaxg10-1	30725.71	0.111	27778.01
2	biaxg10-1b	30082.32	0.088	27196.35
3	biaxg10-4	27099.18	0.020	24499.40
4	biaxg10-5	19005.39	0.313	17182.09
	avg.	26728.15	0.133	24163.96
	st. dev.	5385.46		4868.80
<i>Aluminum, E<sub>constrained theory</sub> = 75,480 MPa</i>				
1	biaxalu1	55441.56	0.265	51416.50
2	biaxalu2	65791.13	0.128	61014.69
3	biaxalu3	61688.46	0.183	57209.88
	avg.	60973.72	0.192	56547.03
	st. dev.	5211.67		4833.30

**Table 8** Summary table listing  $E_{constrained}$  and  $E_{free}$  values derived from warm bi-axial load tests of epoxy, G10, and aluminum test samples, with fractional deviation from the theory values, as well as mean and standard deviation values of the data sets. The  $E_{constrained}$  values were calculated directly from the load test data, by the conventional method. The experimental  $E_{free}$  values were determined by reversing the calculation for the constrained modulus in the experimental model presented in the discussion of the warm bi-axial load test.

<b>Integrated Thermal Contraction Experimental Values (Cold Uni-axial Data)</b>						
<i>trial</i>	<i>filename</i>	<i>gauge</i>	$D\epsilon_{DT\text{gauge-sample}}$	$\epsilon_{DT}$	$\epsilon_{DT}$ (mm/m)	<i>deviation</i>
<i>G10, <math>\epsilon_{DT} = 2.73</math> mm/m</i>						
1	coldg10-1	axial	0.001241	0.001809	1.81	0.337
		lateral	0.000053	0.002997	3.00	0.098
		avg.	0.000647	0.002403	2.40	0.120
		st. dev.	0.000840	0.000840	0.84	
<i>Aluminum, <math>\epsilon_{DT} = 4.40</math> mm/m</i>						
1	coldalu1	axial	-0.002113	0.005163	5.16	0.174
		lateral	-0.002331	0.005381	5.38	0.223
		avg.	-0.002222	0.005272	5.27	0.198
		st. dev.	0.000154	0.000154	0.15	
2	coldalu2	axial	-0.002143	0.005193	5.19	0.180
		lateral	-0.002055	0.005105	5.11	0.160
		avg.	-0.002099	0.005149	5.15	0.170
		st. dev.	0.000062	0.000062	0.06	

**Table 9** Summary table listing  $\epsilon_{\Delta T}$  values derived from the zero-load strain gauge resistance values measured immediately before and after cooling for cold uni-axial load tests on the G10 and aluminum test samples, along with fractional deviation from the theory values, and mean and standard deviation values for each gauge-value pair. The  $\epsilon_{\Delta T}$  values were calculated according to the experimental model presented in the discussion of the cold uni-axial load test, which involved a correction to the apparent thermal strain  $\Delta\epsilon_{DT\text{gauge-sample}}$  registered by the strain gauge following cooling due to differential integrated thermal contraction between the gauge and the test sample over the given temperature range.

## Appendix 4

### Test Fixture Vertical Stress Calibration

Before performing the bi-axial loading test, we performed a calibration of the vertical stress mechanism in the test fixture, which was needed for selecting the precise vertical stresses to be applied in our bi-axial loading tests. Since the amount of pressure created within the test bed depends upon the downward displacement of the upper wedge, which is regulated by thin steel shims sandwiched between the top and bottom plates of the fixture, the aim of our calibration was a functional dependence of vertical stress  $\sigma$ , as read by the capacitance gauge inside the fixture, upon the shim thickness  $s$  used to achieve that stress.

*Experimental Model:* The applied vertical stress is directly dependent upon the downward displacement of the upper wedge, which is given by the reduction in shimming  $\Delta s$  from the critical zero-stress shim value  $S_0$ , determined from experiment, which corresponds to the initial height of the wedge

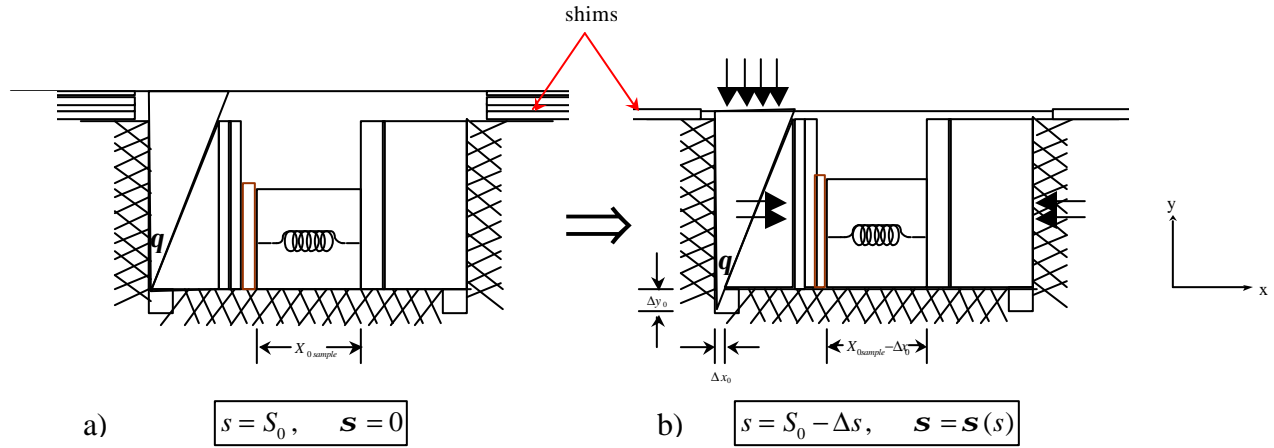


**Figure 1** Mechanical representation of vertical stress mechanism model, first approximation. In this approximation, all elements of the system are perfectly rigid except for the test sample, which receives all of the stress-induced strain. The zero-stress initial state is represented in a) with the zero-stress critical shim value  $S_0$  determined by experiment. The final stress state is represented in b) with shimming reduced by  $\Delta s$ .

above the fixture base. Assuming ideally that all elements of the system are perfectly rigid except for the test sample, then the strain in the sample accounts for all of the vertical stress in the system, i.e.

$$\mathbf{s}_v = E_{sample} \mathbf{e}_{sample} \quad (1)$$

Assigning to our CC vertical and CC horizontal axes the coordinates  $x$  and  $y$ , respectively, as in Figure 1, we have, then,

$$\mathbf{e}_{sample} = \frac{\Delta x_0}{X_{0sample}} \quad (2)$$

where  $X_{0sample}$  is the initial length of the sample in the  $x$ -direction, and  $\Delta x_0$  is the lateral displacement of the lower wedge caused by the downward displacement of the upper wedge. These displacements are related geometrically as

$$\Delta x_0 = \Delta y_0 \tan \theta \quad (3)$$

where  $\theta$  is the wedges' angle of inclination. In a rigid frictionless wedge system, the downward displacement of the upper wedge  $\Delta y_0$  is equal to  $\Delta s$ , the reduction in shimming from the experimentally

determined  $S_0$ . We can therefore, by combining our equations, calculate the vertical stress in terms of known quantities, according to

$$\mathbf{s}_v = \frac{E_{sample} \Delta s \tan \mathbf{q}}{X_{0sample}} \quad (4)$$

In a non-ideal system like our apparatus, in which stress-induced strain is distributed throughout the system, according to the varying stiffness of its elements, this first approximation is inadequate. We must also consider the case in which elastic energy is spread throughout the system such that other elements undergo strain, as illustrated in Figure 2.

Since the stainless steel test fixture has a finite stiffness, the vertical stress inside the test bed induces a strain in the fixture walls dependent upon the elastic modulus of steel, thus distributing part of the total vertical strain into the fixture according to the ratio of the sample modulus to the fixture modulus. Thus, the strain in the sample no longer accounts for all of the stress in the system. Since our measurement is concerned only with the portion of total stress acting on the test sample, we must correct our vertical stress calculation to account for this lost stress. In the new scenario, the total stress,

$$\mathbf{s}_v = E_{sample} \mathbf{e}_{sample} + E_{steel} \mathbf{e}_{fixture} \quad (5)$$

The effective stress on the sample, then, is

$$\frac{1}{2} \mathbf{s}_v \leq \mathbf{s}'_v = E_{sample} \mathbf{e}_{sample} \leq \mathbf{s}_v \quad (6)$$

for  $E_{sample} \leq E_{fixture}$ . For  $E_{sample} = E_{fixture}$ , the stress is distributed evenly between both parts of the system, and  $\sigma'_v = \sigma_v/2$ ; for  $E_{sample} \ll E_{fixture}$ , we return to the first approximation, so that  $\sigma'_v = \sigma_v$ . In order to correct for the fixture deformation in the vertical direction, then, we simply multiply our calculated vertical stress by a correction factor

$$\mathbf{s}'_v = \mathbf{s}_v \left( \frac{1}{1+f} \right) \quad (7)$$

where

$$f = \frac{E_{sample}}{E_{steel}} \quad (8)$$

This factor gives us the correct boundary conditions. As  $E_{sample} \rightarrow E_{fixture}$ , the correction factor approaches one half, so that the total vertical stress is evenly divided between the sample in the test bed and the fixture itself. Conversely, for  $E_{sample} \ll E_{fixture}$ , the correction factor approaches one, which is what is expected for a system which is perfectly rigid with respect to the sample in the vertical direction.

Stress is also distributed along the horizontal direction (CC frame), within the wedge system, which is pressurized between the fixture top plate and base (see Figure 2). Because of these elasticities in the horizontal direction, the  $\Delta y_0 = \Delta s$  condition no longer holds. The downward displacement of the lower end of the upper wedge is less than the displacement of the upper portion of the wedge, due to internal strain along its length. As a result, we instead have the condition

$$\Delta y_1 = \Delta s - \Delta y_2 - \Delta y_3 - \Delta y_4 \quad (9)$$

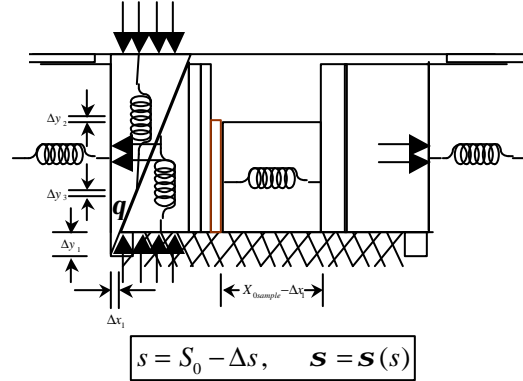


**Figure 2** Mechanical representation of vertical stress mechanism model, second approximation. Small deformations along the chain of stress have a large effect upon the sample strain, thereby significantly modifying the first model of the system. Springs on the fixture walls represent elasticity of the stainless steel fixture in the vertical direction, while springs on the wedges represent horizontal elasticities within the wedge system.

where  $\Delta y_1$  is the real downward displacement of the lower portion of the upper wedge,  $\Delta y_2$  is the horizontal deformation due to strain in the upper wedge,  $\Delta y_3$  is the horizontal deformation due to strain in the lower wedge, and  $\Delta y_4$  is the horizontal deformation due to buckling of the fixture top plate, as illustrated in Figure 3. These deformations can be expressed easily in terms of elastic uniaxial loading, as

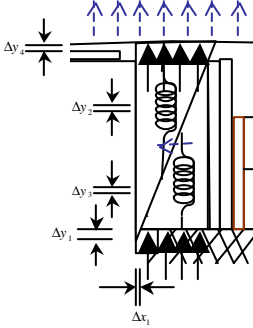


**Figure 3** Strain in the fixture top plate enables an upward displacement of the upper wedge, thereby subtracting from the wedge's displacement at the bottom, and thus the deformation of the sample.

$$\Delta y_2 = \frac{\sigma_y Y_{0copper}}{E_{copper}} \quad (10)$$

$$\Delta y_3 = \frac{\sigma_y Y_{0steel}}{E_{steel}} \quad (11)$$

$$\Delta y_4 = \frac{\sigma_y Y_{0top\_plate}}{E_{steel}} \quad (12)$$

where  $Y_{0copper} = 0.875$  inches,  $Y_{0steel} = 0.787$  inches, and  $Y_{0top\_plate} = 1.500$  inches are the initial horizontal lengths of the upper copper wedge, the lower steel wedge, and the fixture top plate, respectively,  $E_{copper} = 120,000$  MPa and  $E_{steel} = 210,000$  MPa are their respective elastic moduli, and  $\sigma_y$  is the horizontal stress in the wedges. Combined with our original geometric relation for  $\sigma_x$  (not including the  $\Delta y_0 = \Delta s$  condition), to which we add linearly a term accounting for strain in the capacitance gauge, which is in series with the sample,

$$\Delta y_1 = \frac{\sigma_x X_{0sample}}{E_{sample} \tan q} + \frac{\sigma_x X_{0cap\_gauge}}{E_{kaptan} \tan q} \quad (13)$$

with  $X_{0cap\_gauge} = 0.020$  inches and  $E_{kaptan} = 3,000$  MPa, these expressions gives us the equation

$$\Delta s = \frac{\sigma_x X_{0sample}}{E_{sample} \tan q} + \frac{\sigma_x X_{0cap\_gauge}}{E_{kaptan} \tan q} + \frac{\sigma_y Y_{0copper}}{E_{copper}} + \frac{\sigma_y Y_{0steel}}{E_{steel}} + \frac{\sigma_y Y_{0top\_plate}}{E_{steel}} \quad (14)$$

Since we have geometrically,

$$F_x = F_y \sin q \cos q \quad (15)$$

we express our pressures in terms of forces by dividing out the pressurized areas, giving

$$\Delta s = \frac{F_x}{A_x \tan q} \left( \frac{X_{0sample}}{E_{sample}} + \frac{X_{0cap\_gauge}}{E_{kaptan}} \right) + \frac{F_y}{A_y} \left( \frac{Y_{0copper}}{E_{copper}} + \frac{Y_{0steel}}{E_{steel}} + \frac{Y_{0top\_plate}}{E_{steel}} \right) \quad (16)$$

where  $A_x = 0.800$  inch x  $0.575$  inch =  $0.460$  in  $inch^2$  is the sample/capacitance gauge surface over which the vertical stress is distributed, and  $A_y = 1.800$  inch x  $0.464$  inch =  $0.835$   $inch^2$  is the top surface of the upper wedge over which the horizontal stress is distributed. Then we substitute  $F_x$  for  $F_y$  in Eq. 16 according to Eq. 15, yielding

$$\Delta s = \frac{F_x}{A_x \tan q} \left( \frac{X_{0sample}}{E_{sample}} + \frac{X_{0cap\_gauge}}{E_{kaptan}} \right) + \frac{F_x}{A_y \sin q \cos q} \left( \frac{Y_{0copper}}{E_{copper}} + \frac{Y_{0steel}}{E_{steel}} + \frac{Y_{0top\_plate}}{E_{steel}} \right) \quad (17)$$

Finally, then, including the vertical fixture deformation correction factor, we have Equation 18:

$$\sigma_x = \frac{\Delta s}{A_x} \left[ \frac{1}{A_x \tan q} \left( \frac{X_{0sample}}{E_{sample}} + \frac{X_{0cap\_gauge}}{E_{kaptan}} \right) + \frac{1}{A_y \sin q \cos q} \left( \frac{Y_{0copper}}{E_{copper}} + \frac{Y_{0steel}}{E_{steel}} + \frac{Y_{0top\_plate}}{E_{steel}} \right) \right]^{-1} \left( \frac{1}{1+f} \right)$$

an expression for the vertical stress on the sample in terms of known quantities, which takes account of both horizontal and vertical (CC frame) elasticities in the mechanism.

With all of these corrections made, we expect the following relations for the three test samples we calibrated for vertical pre-stressing:

$$\mathbf{s} = -2763.1s + \mathbf{s}(0), \quad E = E_{epoxy} \quad (19)$$

$$\mathbf{s} = -9526.2s + \mathbf{s}(0), \quad E = E_{G10} \quad (20)$$

$$\mathbf{s} = -12718s + \mathbf{s}(0), \quad E = E_{aluminum} \quad (21)$$

with  $\sigma(0)$  the pressure expected on the sample at  $s = 0$ .

Pressure was read primarily from the capacitance gauge, though it was checked also with the strain registered by the test sample strain gauges.

*Preparation:* In order to facilitate performance of the calibration, which did not require placement of the fixture inside the load cell, a temporary work table was positioned next to the load cell; this enabled us to avoid a cumbersome transfer of the heavy fixture between preparation and test stands by providing a usable work space with proximity to the capacitance gauge circuit used in measurement. The test fixture's preparation fixture was secured with vices to the mobile worktable. The test fixture was prepared in the same way as for a bi-axial loading test, except never removed from the preparation fixture during the calibration, since the capacitance gauge could be connected directly to the measurement circuit from the work table. The measurement was performed on epoxy, G10, and aluminum samples.

*Measurement:* Since the measurement software is programmed to take measurements keyed by stress registered in the load cell, but the load cell is not employed in the calibration (which requires zero horizontal load), a special addition was made to the program permitting capacitance and resistance measurements with no horizontal load.<sup>10</sup> With the capacitance and strain gauges connected to their respective circuits, the calibration sequence is initialized in the same way as in the bi-axial loading test. To "trick" the program into registering a load, which in turn triggers measurements, a special "Boolean" switch is turned upwards, and the number  $-0.0055$  is inputted in the "number" panel above it, along with a 1.000 inch  $\times$  0.575 inch pressurizing surface; this registers a load of approximately 8700 psi in the program, which, set to take measurements at intervals of 500 psi, proceeds to record 18 resistance and capacitance readings from meters monitoring the circuits, all at the given stress inside the fixture. Following each measurement, the fixture is disassembled and then reassembled with a different number of shims to determine the next data point in the calibration. (Note: it is advisable to unplug the capacitance gauge cable between measurements to avoid breaking the cable during the bolting process.) Measurements were made in a shim range of 0.000 inch  $< s <$  0.113 inch, proceeding from high to low shim (i.e. by increasing load); though the entire shim range was investigated during the epoxy calibration, a smaller range was studied for G10 and aluminum, since steeper pressure curves were expected.

*Data Analysis and Results:* For each measurement, the program outputs a set of 18 capacitance values, measured in nF, and resistance values, measured in ohms. Each set of values is averaged, and subsequent analysis is performed on the resultant mean value. While the recorded resistance values exhibited an acceptable regularity, preliminary analysis of the data revealed some peculiarities in the capacitance readings. The first capacitance value in each data set is a superfluous "initializing value" significantly below the other values in the set and must be discarded on a statistical basis. Also, a high level of uncertainty was observed in the capacitance data, which lead to a high level of uncertainty in our initial calibration measurements (see Figure 4, next page). Figure 5 demonstrates how the significant fluctuation in our capacitance readings, with an average range of 0.02 nF, required the adaption of our measurement procedure to a Boolean setting which would ensure a sufficient number of data points to achieve a normal distribution in the values of each measurement. With this change, we improved our confidence level in the mean capacitance values to  $\pm 0.002$  nF.

Mean capacitance values are transformed to stress values, in units of MPa, according to our calibration of the capacitance gauge:

$$C = 0.0003666\mathbf{s} + C_0 \quad (CC10SC1)$$

$$C = 0.0003725\mathbf{s} + C_0 \quad (CC10SC2)$$

---

<sup>10</sup> Adaption made by L. Elementi in August, 2001.

where  $C$  is the capacitance value in nF,  $\sigma$  is the pressure in MPa, and  $C_0$  is a zero load capacitance value determined at the beginning of the measurement. Vertical strain is calculated from resistance values registered by the vertical strain gauge, and vertical stress is calculated from the strain and modulus of the sample. The mean stress values from both the capacitance and the strain gauges are plotted against shimming, with associated statistical errors from each value's data set. In addition, vertical and horizontal sample strain are plotted against the corresponding pressure values of the capacitance gauge, to check for irregularities in the loading pattern, such as the stress gradients which were encountered in the uniaxial loading tests.

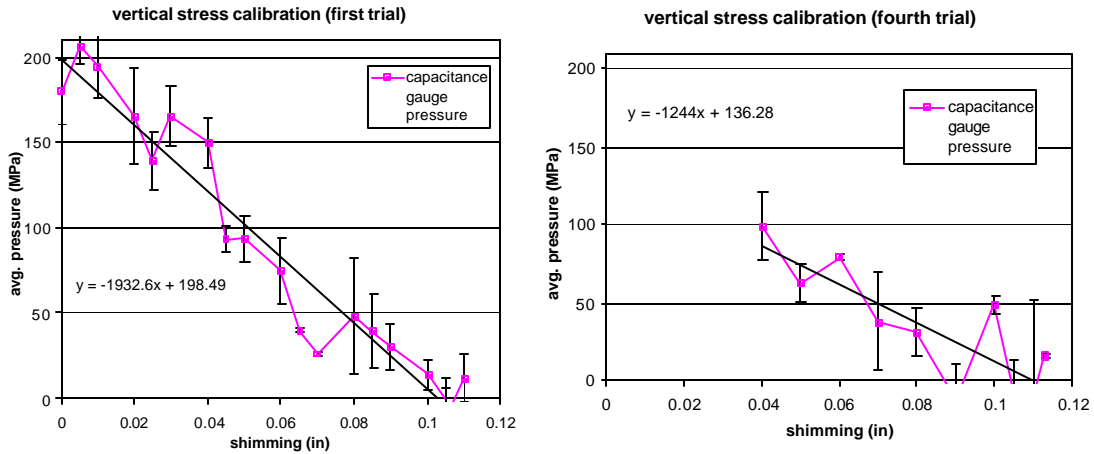


**Figure 4** First and fourth trials of vertical stress mechanism calibration possessed unacceptable fluctuation in the mean values and their associated error ranges. (Each point on the plot represents the mean value of the data set recorded for the given stress.)

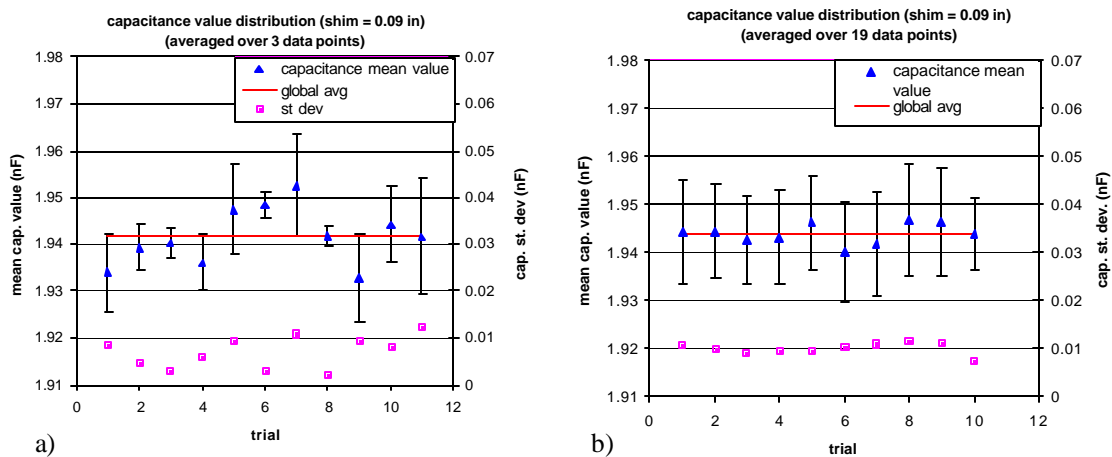


**Figure 5** Distribution study of capacitance readings from the measurement apparatus, using two variations of the measurement procedure. In the first variation a) the Boolean number = -0.0011 and the values are averaged over 3 data points; this results in significant variation in the uncertainty of each data set and a standard deviation among the mean values of 0.006 nF from the global average. In the second variation b) the Boolean number = -0.0055 and the values are averaged over 19 data points; this regularizes the uncertainty of the data sets and stabilizes the mean values, yielding a standard deviation among the mean values of 0.002 nF from the global average.

Several improvements were made to the experimental set-up and procedure during the course of the first set of calibration measurements, with the epoxy sample, in response to problematic results which gave rise to improved understanding of the system. For example, 1) a systematic discrepancy between the capacitance value obtained by manual acquisition through the LCR meter and the value obtained through

the data acquisition program left us uncertain of the real capacitance of the capacitance gauge. However, since the pressure calibration of the gauge depends upon  $\Delta C/\Delta\sigma$ , rather than on absolute  $C$  values, this uncertainty posed no problem to our measurement of pressure with the capacitance gauge; a zero-load  $C_0$  value to be measured at the outset of each measurement completed the terms necessary for calculation of the pressure from our capacitance values. 2) Our first measurement, in which the system became rigidly fixed in a pressurized state, led to the addition of acrylic lubricant to the wedge surfaces, since without it, the high pressure within the fixture caused metallic bonding between their surfaces, thus preventing them from sliding back to their initial state once the fixture was unbolted. 3) Encounter with large variances in the capacitance values during our first four calibration trials led to the capacitance value distribution study displayed in Figure 5, whose conclusion yielded a marked improvement in the linearity of our capacitance values with changing pressure. This can readily be observed by comparison of results in Figure 4 with those in Figure 6, which shows data from the 5<sup>th</sup> through 9<sup>th</sup> trials of the epoxy vertical pressure

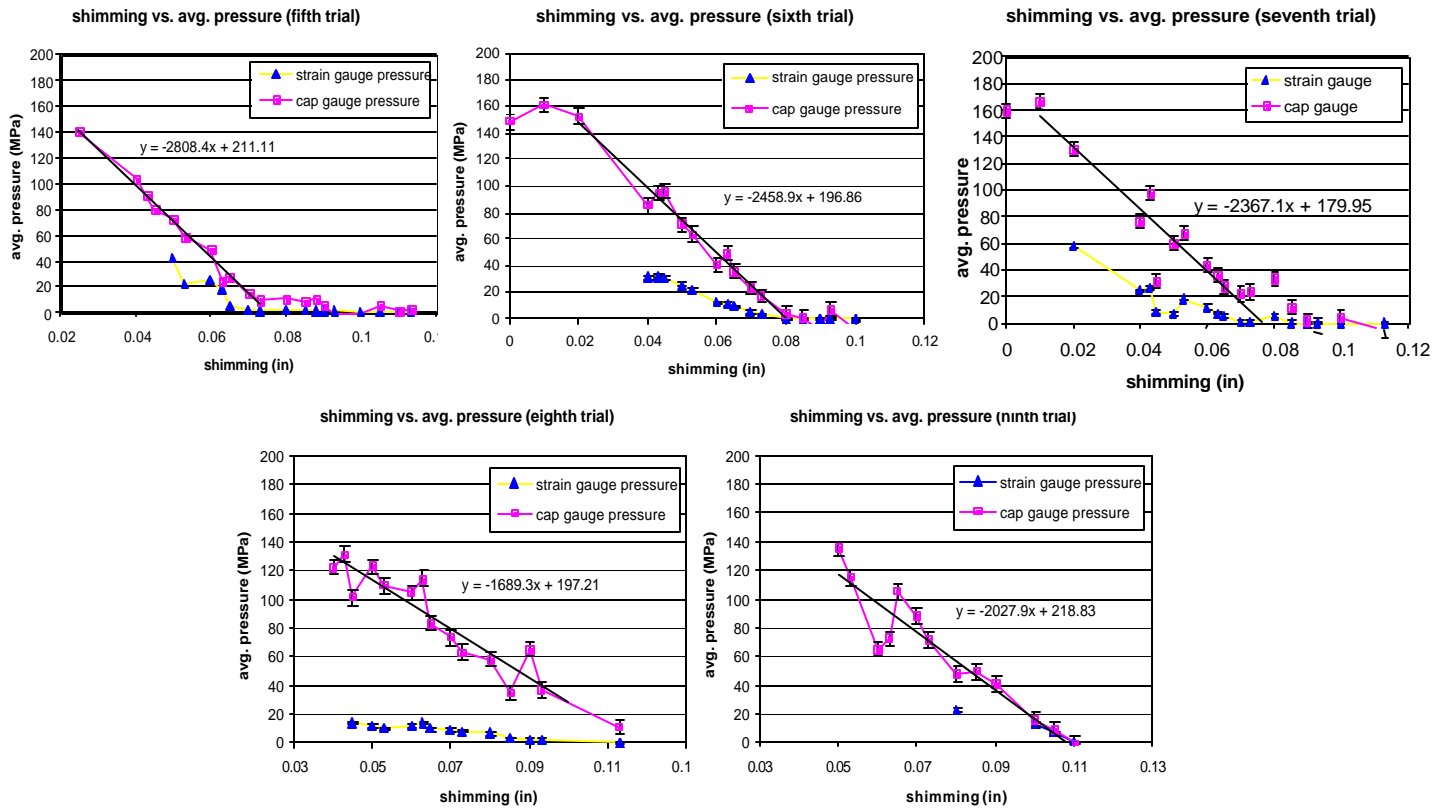


**Figure 6** Fifth through ninth trials of fixture vertical stress calibration with epoxy sample. Though broadly linear, capacitance gauge data fluctuates significantly, despite being averaged over 20 values. Note: eighth and ninth trials were performed with fuji paper inserts to study the source of discrepancy between capacitance gauge and strain gauge readings; hence the translation of the curve from  $S_0 = 0.08$  in to  $S_0 = 0.11$  in.

calibration. 4) Linearity of the capacitance values was further improved in subsequent calibration measurements with the aluminum and G10 samples, when we discovered the importance of the initial corner bolt tightening phase (as described in the biaxial measurement procedure) to achieving uniformly distributed pressures within the fixture. This improvement is evident in careful comparison between capacitance gauge results in Figure 6 and Figure 7, which shows data from our G10 and aluminum measurements.

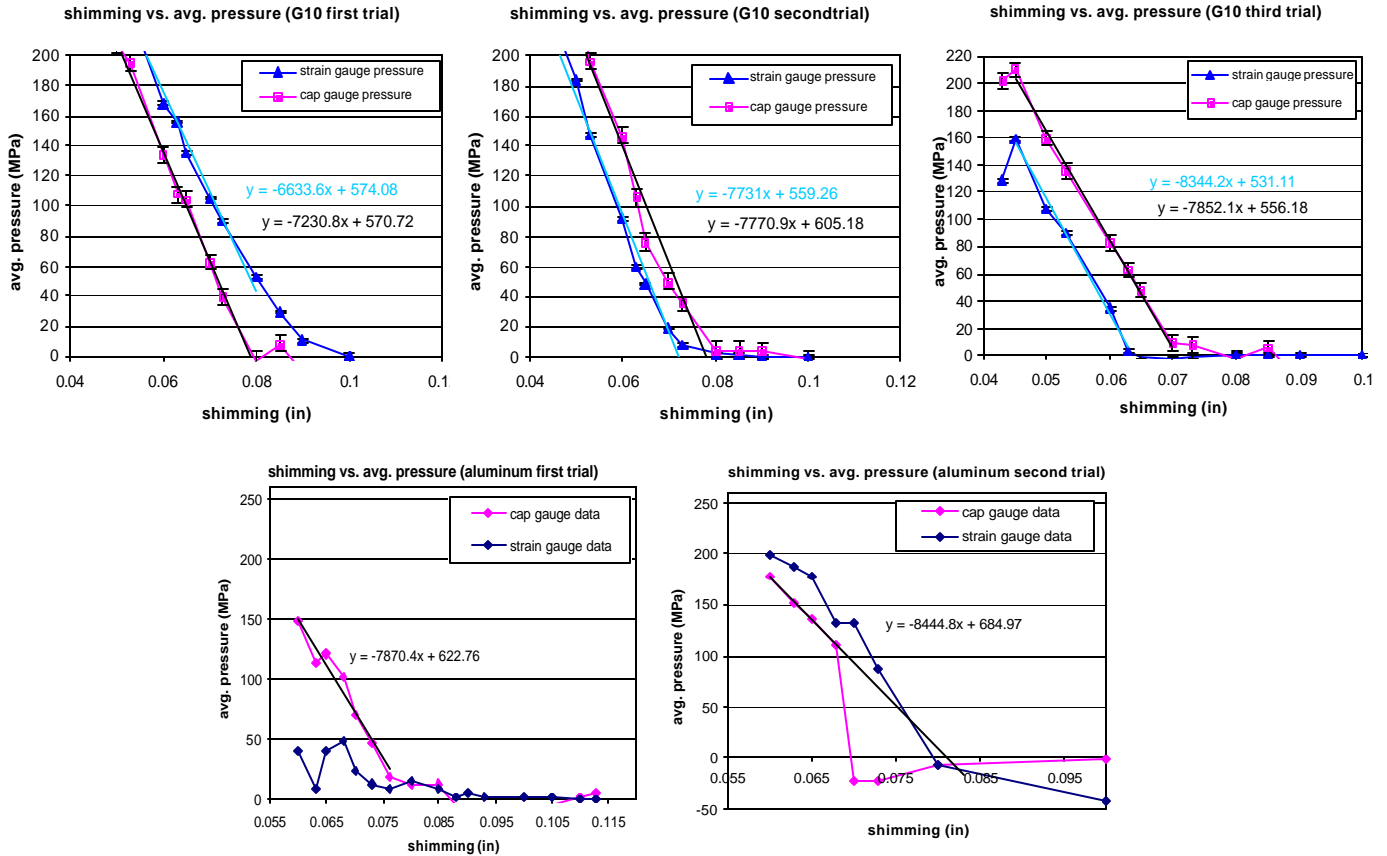


**Figure 7** First through third trials of vertical stress calibration for G10 sample, and first and second trials for aluminum sample. The linearity of the capacitance gauge values is significantly improved due to an improved initial bolting procedure. Note: the G10 measurements were performed after the aluminum measurements.

The measurements displayed in Figures 6 and 7 showed sufficient consistency to determine conclusive calibration relations for each sample. All of the results are plotted below and combined into single plots in Figures 8, 9, and 10.

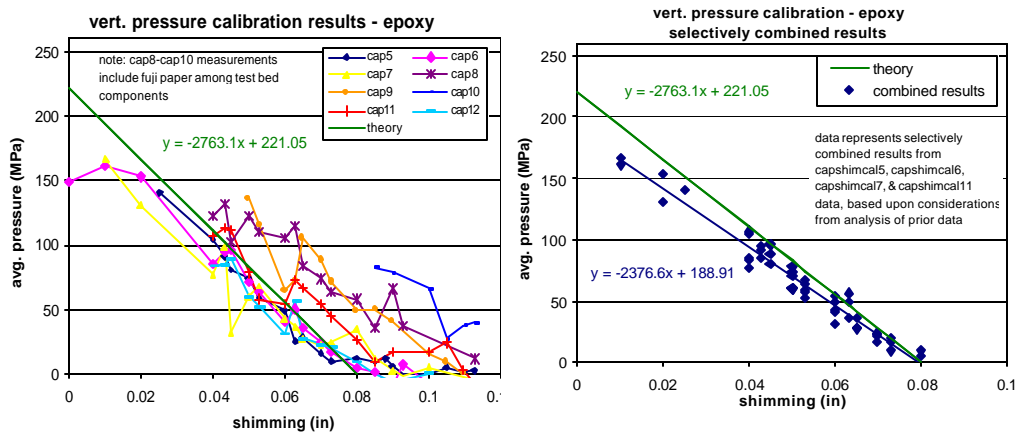


**Figure 8** Combined results of vertical stress calibration for epoxy sample.

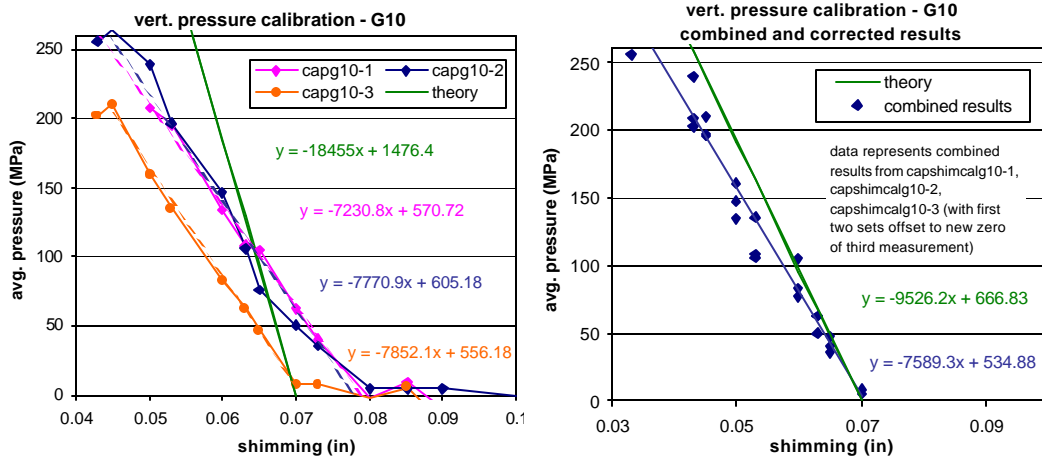


**Figure 9** Combined results of vertical stress calibration for G10 sample.

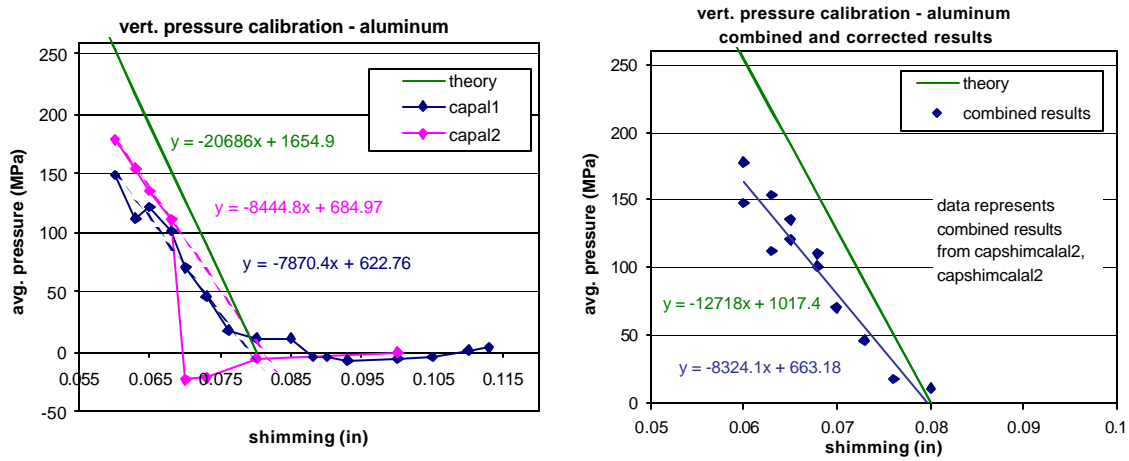


**Figure 10** Combined results of vertical stress calibration for aluminum sample.

From these plots we generated the following calibration relations.

$$s = -2376.6s + 188.91, \quad E = E_{epoxy} \quad (22)$$

$$s = -7589.3s + 534.88, \quad E = E_{G10} \quad (23)$$

$$s = -8324.1s + 663.18, \quad E = E_{aluminum} \quad (24)$$

The experimental calibration slopes varied from the theoretical slopes by 14.0% for epoxy, 20.3% for G10, and 34.5% for aluminum. However, the calibrations proved highly effective in predicting vertical stresses during the biaxial measurements. A plot of the slopes vs. the modulus is displayed in Figure 11. The remaining discrepancy between the theoretical values and experimental values is most likely rooted in unaccounted factors in the theoretical model, particularly friction in the moving elements—between the wedge surfaces, and between the wedges and the fixture walls. The theory may be corrected to the experimental curve by correcting the model with a modulus-dependent factor of proportionality. If we write the equation for the theoretical model of the vertical stress in the form

$$s(\Delta s) = B\Delta s \quad (25)$$

then we make the correction based on experimental results

$$s(\Delta s) = B\Delta s(0.8 - 1.5 \times 10^{-6} E) \quad (26)$$

which leaves us finally with an equation for the vertical pre-stress with perfect conformity to experimental results.

Despite consistent capacitance gauge results through the course of the measurements, Figures 6 and 7 reveal a troubling discrepancy between pressures read by the capacitance gauge and that seen by the strain gauge affixed to the sample. Though not critical to determining the stress applied to the sample by the fixture's vertical stress mechanism, which was the primary aim of the fixture calibration, this discrepancy would significantly distort results during biaxial loading. As Figure 12 illustrates, the mechanism consistently produced asymmetric stress upon the sample during the first set of epoxy calibrations, with one strain gauge registering the expected stress and other registering no stress. This pattern differed from the understood behaviour associated with stress concentration observed in uniaxial load tests. In order to study the behaviour, stress-sensitive fuji paper was inserted throughout the stress chain between the elements of the test bed during calibration trials eight through ten. While showing no stress concentration, the fuji paper revealed, upon closer analysis, the cause of the discrepancy. The sample surface under pressure

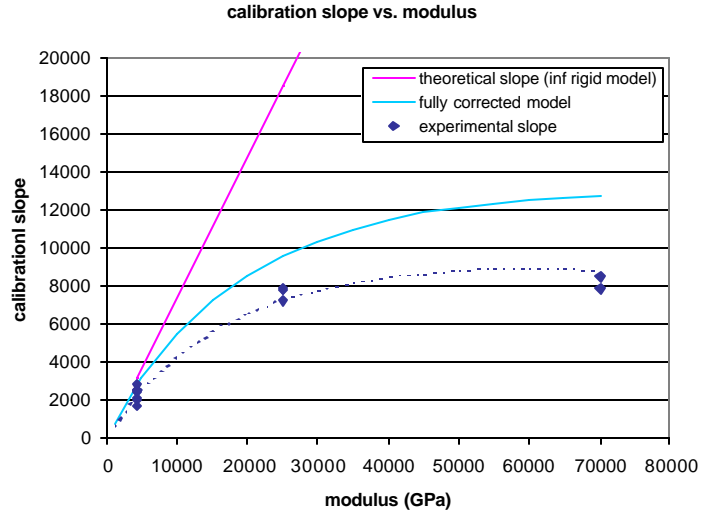


**Figure 11** Comparison of calibration slope vs. modulus curves for the theoretical model (first approximation) as defined by Eq. 4, the corrected theoretical model defined by Eq. 18, and the experimental results, listed in Eqs. 22-24. The remaining discrepancy between theory and results may be due to the uncalculated stress loss due to friction between the wedges.

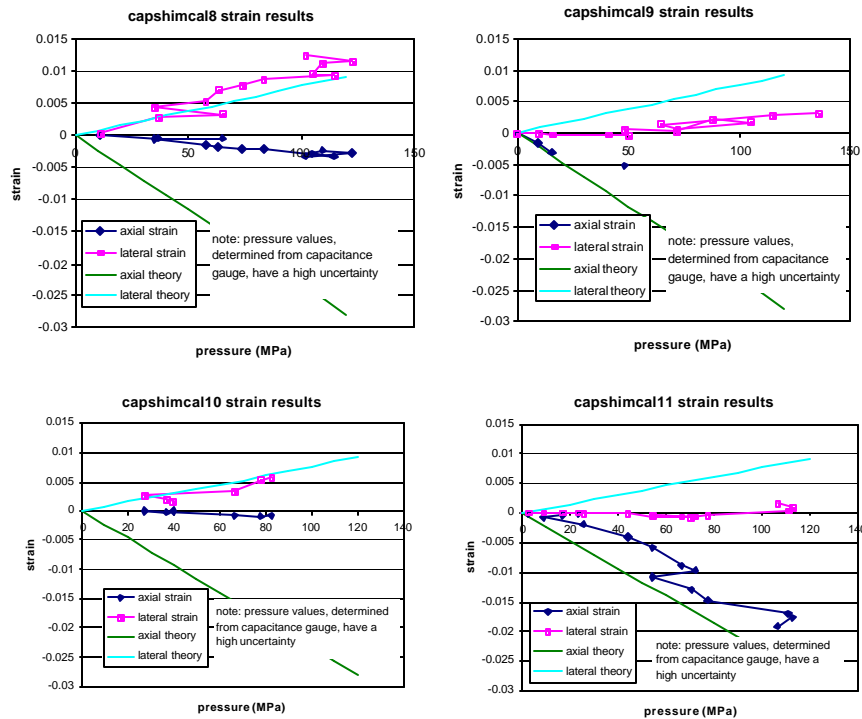


**Figure 12** Stress vs. strain plots for trials eight through eleven of the vertical stress calibration for the epoxy sample, with strain values plotted against stress values registered by the capacitance gauge. The sample is rotated 90 degrees between the tests, so the gauges switch orientation, demonstrating that a gauge on one side of the sample consistently observes no pressure while the other gauge observes the same pressure as that read by the capacitance gauge.

proved to be longer than the cap gauge surface transmitting pressure to the sample in the chain of stress, by a critical amount of 0.200 inches, leaving one end of the sample unpressurized and thus registering no stress in the associated strain gauge. This problem was resolved by cutting the sample to the same length as the capacitance gauge, yielding finally a satisfactory result in the twelfth trial of the calibration with the epoxy sample, as well as the aluminum and G10 calibrations following it (see Figure 13).

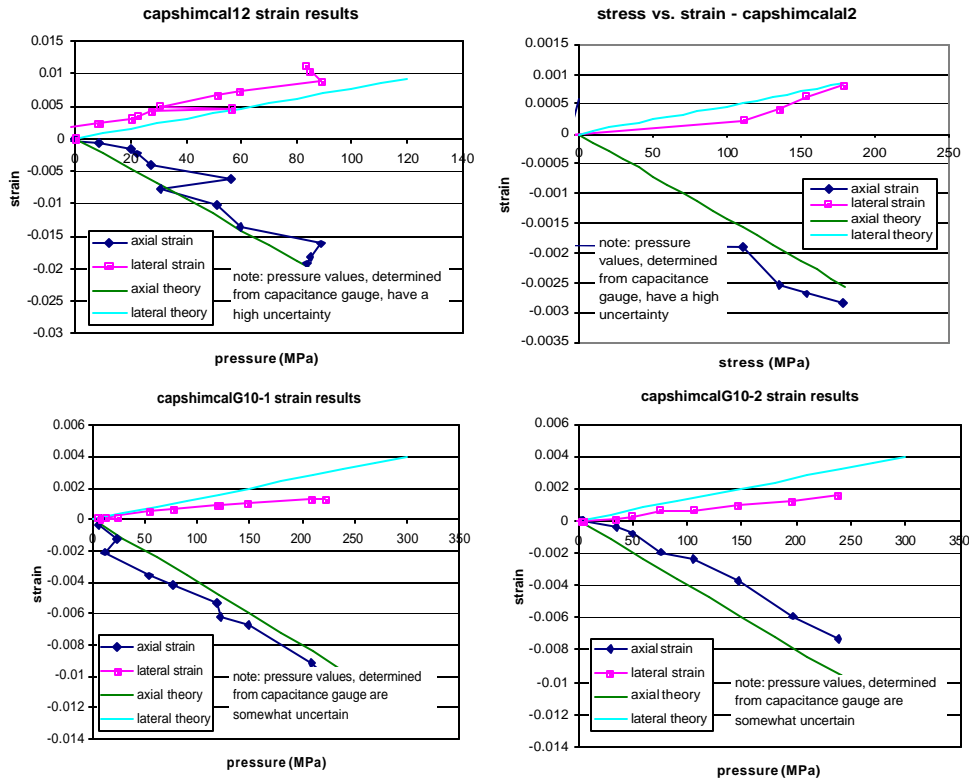


**Figure 13** Stress vs. strain plots for trial twelve of vertical stress calibration for the epoxy sample, trial two of calibration for the aluminum sample, and trials one and two of calibration for the G10 sample—all performed with samples recut to length of capacitance gauge, following fuji paper study. Strain gauges register stress as expected, demonstrating resolution of the discrepancy in initial epoxy calibration trials. This improvement may be compared with strain gauge data in Figure 7.

With these symmetric strain results achieved in the calibration of the fixture's vertical stress mechanism, the mechanism seemed adequately debugged to proceed with biaxial load tests.<sup>11</sup>

<sup>11</sup> A new, but different asymmetry arose in the vertical stress mechanism during the course of biaxial load tests, posing significant problems for the measurements. This asymmetry is discussed at length in Appendix 5.

## Appendix 5

### Vertical Stress Asymmetry from Fixture Deviation

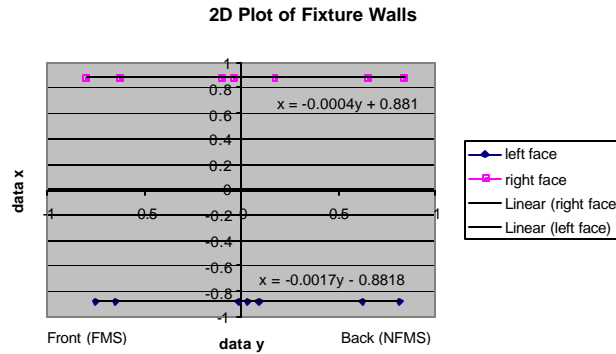


**Figure 2** Two-dimensional plot of quality control data for measurement of parallelism between fixture walls.

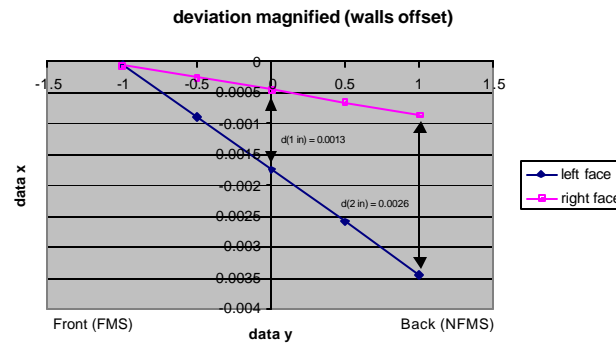


**Figure 3** Quality control data, showing deviation from parallelism, displayed to scale.

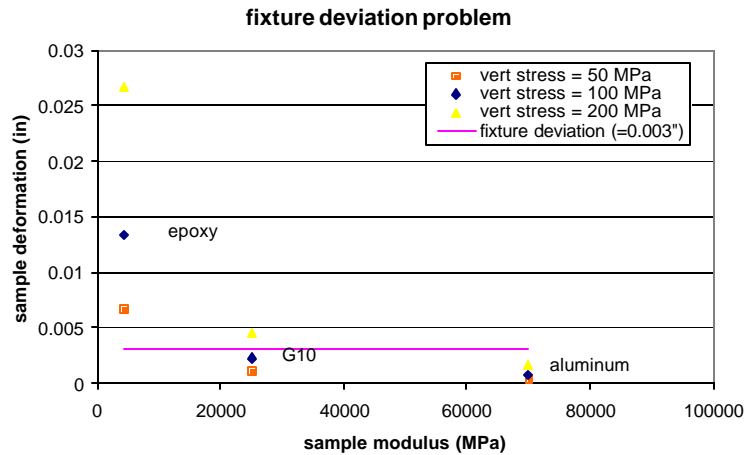


**Figure 4** Modulus-dependent effect of fixture deviation upon strain gauge readings in vertical stress.

## Appendix 6

### Experimental Model for Change in Bi-axial Pre-stress from Cooling to Liquid Helium Temperature

A calibration of the fixture's vertical stress mechanism can be solved analytically at  $T = 4.2 \text{ K}$  with a few additions and adjustments to the model already presented in Appendix 4 for the vertical stress as a function of shimming at  $T = 300 \text{ K}$ . The model for the cold vertical pre-stress was investigated as a precise means to determining the expected pre-stress at  $T = 4.2 \text{ K}$  as a function of shimming, or construed differently, the expected cold pre-stress as a function of warm pre-stress and thus, the expected change in pre-stress following cool-down from a given warm pre-stress. This prediction is critical to effective execution of the cold bi-axial loading test.

*Review of warm stress model:* In the warm vertical stress calibration model, several differential dimensional magnitudes in the system's relevant axes—the horizontal (CC) y-axis and the vertical (CC) x-axis—were specified by mechanical equations, which described the system under stress, and related together by geometric constraints to the critical shimming variable,  $\Delta s$ . Figure 1 illustrates all of these magnitudes in a diagram of the system in a pressurized mechanical equilibrium, as prescribed by the fixture design. Equations 1-3 provide the essential constraints relating these quantities.

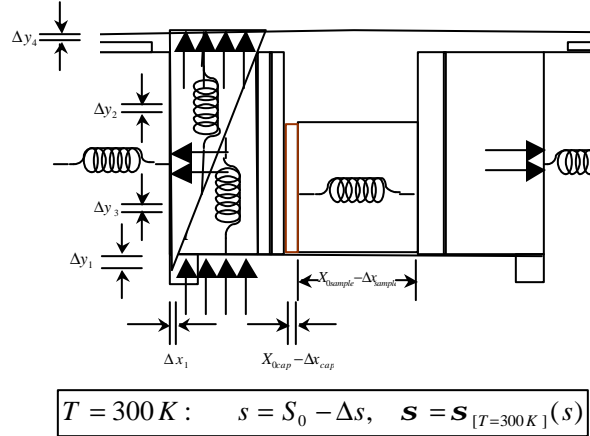


**Figure 1** Mechanical representation of the vertical stress mechanism in equilibrium at room temperature, showing dimensional magnitudes defined by the system's mechanical stresses and the geometric constraints relating them. This diagram illustrates the mechanical basis of the model for the warm calibration of the fixture's vertical stress as a function of regulating shimming  $s$ .

*Review of warm stress model:* In the warm vertical stress calibration model, several differential dimensional magnitudes in the system's relevant axes—the horizontal (CC) y-axis and the vertical (CC) x-axis—were specified by mechanical equations, which described the system under stress, and related together by geometric constraints to the critical shimming variable,  $\Delta s$ . Figure 1 illustrates all of these magnitudes in a diagram of the system in a pressurized mechanical equilibrium, as prescribed by the fixture design. Equations 1-3 provide the essential constraints relating these quantities.

$$\Delta y_1 = \Delta s - \Delta y_2 - \Delta y_3 - \Delta y_4 \quad (1)$$

$$\Delta x_1 = \Delta x_{sample} + \Delta x_{cap\_gauge} \quad (2)$$

$$\Delta x_1 = \Delta y_1 \tan \theta \quad (3)$$

$\Delta s$ ,  $\Delta y_1$ , and  $\Delta x_1$  are merely dimensional features of the system, while the rest of the quantities are defined as mechanical deformations due to axial stresses in the system. The mechanical deformations in the y-direction were related by Hooke's Law to the corresponding axial stress,

$$\Delta y_2 = \frac{s_y Y_{0copper}}{E_{copper}} \quad (4)$$

$$\Delta y_3 = \frac{s_y Y_{0steel}}{E_{steel}} \quad (5)$$

$$\Delta y_4 = \frac{s_y Y_{0top\_plate}}{E_{steel}} \quad (6)$$

and likewise for the mechanical deformations in the x-direction

Element	$X_0/Y_0$ (inches)	$E_{[T=300K]}$ (MPa)
copper wedge	0.875	120,000
steel wedge	0.787	210,000
steel top plate	1.500	210,000
cap gauge	0.020	3,000
sample	0.575	varies

**Table 10** Essential quantities employed in the calculation of the fixture's vertical pre-stress at room temperature, including the fixture elements' initial dimensions before deformation and their room temperature modulus values.

$$\Delta x_{sample} = \frac{\mathbf{s}_x X_{0sample}}{E_{sample}} \quad (7)$$

$$\Delta x_{cap\_gauge} = \frac{\mathbf{s}_x X_{0cap\_gauge}}{E_{kapton}} \quad (8)$$

Table 1 provides the set of constants involved in each of these equations. Combining Equations 1 and 2 by means of Equation 3, and employing the geometric relation by which the wedges relate forces in the two directions,

$$F_x = F_y \sin \mathbf{q} \cos \mathbf{q} \quad (9)$$

we derived Equation 10, an expression for the vertical stress in terms of the shimming variable and known quantities

$$\mathbf{s}_{x\_warm} = \frac{\Delta s}{A_x} \left[ \frac{1}{A_x \tan \mathbf{q}} \left( \frac{X_{0sample}}{E_{sample}} + \frac{X_{0cap\_gauge}}{E_{kapton}} \right) + \frac{1}{A_y \sin \mathbf{q} \cos \mathbf{q}} \left( \frac{Y_{0copper}}{E_{copper}} + \frac{Y_{0steel}}{E_{steel}} + \frac{Y_{0top\_plate}}{E_{steel}} \right) \right]^{-1} \left( \frac{1}{1+f} \right)$$

with  $A_x = 0.460 \text{ inch}^2$  and  $A_y = 0.835 \text{ inch}^2$ , surface factors introduced in connection with the force conversion, and the last factor, with

$$f = \frac{E_{sample}}{E_{steel}} \quad (11)$$

a correction factor accounting for vertical strains in the fixture. Equation 10 gave us a linear relation between vertical stress and shimming of the form

$$\mathbf{s}(\Delta s) = B \Delta s$$

$$\mathbf{s}(s) = -Bs + BS_0 \quad (12)$$

where  $B = B(E_{sample})$  is the constant of proportionality between the fixture's vertical stress  $\sigma$  and shimming  $s$ . Finally, following the fixture calibration measurements at room temperature for materials of three different moduli, detailed in Appendix 4, a modulus-dependent correction, based on experiment, was introduced to the vertical stress model

$$B_{warm} = B \times (0.8 - 1.5 \times 10^{-6} E) \quad (13)$$

establishing the model as a highly precise and dependable tool for predicting vertical stress in the bi-axial test fixture at room temperature.

*Cold stress model:* For a cold vertical stress calibration model, determining the vertical stress in the fixture as a function of shimming, we consider a mechanical equilibrium of the same system following cool-down to 4.2 K. In this system, stress is applied to elements, which have a greater stiffness, since the modulus of all materials increases as temperature decreases, but reduced initial dimensions, since all of the elements undergo thermal contraction during the cooling process. In addition, differential thermal strains between some of the elements and the fixture result in changes to the constraint equations.

The new mechanical equilibrium is illustrated in Figure 2, and the new constraint relations are given by Equations 14 and 15 (with the

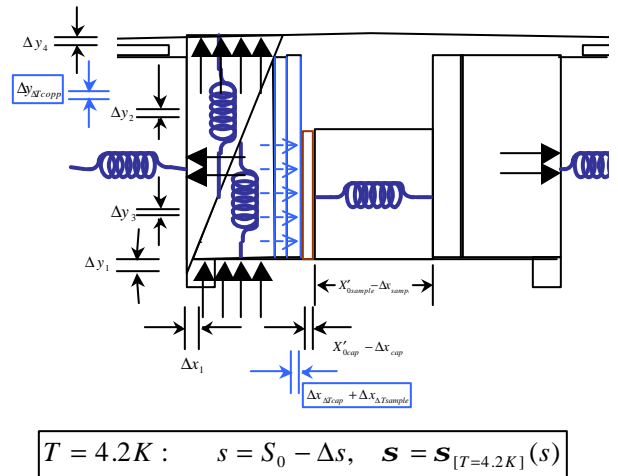


**Figure 2** Mechanical representation of the vertical stress mechanism in equilibrium at 4.2 K. While some of the elements, including the top wedge, the cap gauge, and the test sample contract with respect to the fixture—serving to relax the system—the stiffness of the springs in the diagram (representing the moduli of the materials) increases, thereby increasing the tension between the elements. The precise net effect of these varying contributions to the vertical stress cannot be determined without a complete solution of the mechanical problem.

simple geometric relation of Equation 2 remaining the same).

$$\Delta y'_1 = \Delta s' - \Delta y'_2 - \Delta y'_3 - \Delta y'_4 - \Delta y_{\Delta Tcopper} \quad (14)$$

$$\Delta x'_1 = \Delta x'_{sample} + \Delta x'_{cap\_gauge} + \Delta x_{\Delta Tsample} + \Delta x_{\Delta Tcap\_gauge} \quad (15)$$

where

$$\Delta y_{\Delta Tcopper} = Y_{0copper} \Delta \mathbf{e}_{\Delta Tcopper}, \quad \Delta \mathbf{e}_{\Delta Tcopper} = \mathbf{e}_{\Delta Tcopper} - \mathbf{e}_{\Delta Tsteel} \quad (16)$$

$$\Delta x_{\Delta Tsample} = X_{0sample} \Delta \mathbf{e}_{\Delta Tsample}, \quad \Delta \mathbf{e}_{\Delta Tsample} = \mathbf{e}_{\Delta Tsample} - \mathbf{e}_{\Delta Tsteel} \quad (17)$$

$$\Delta x_{\Delta Tcap\_gauge} = X_{0cap\_gauge} \Delta \mathbf{e}_{\Delta Tcap\_gauge}, \quad \Delta \mathbf{e}_{\Delta Tcap\_gauge} = \mathbf{e}_{\Delta Tcap\_gauge} - \mathbf{e}_{\Delta Tcap\_gauge} \quad (18)$$

are the differential thermal strains between the non-steel elements and the steel fixture, due to non-zero differences between the thermal contraction of these elements and the fixture. The remaining mechanical deformations, though carried over from the original model for warm vertical pre-stress, are changed as well, since the warm modulus values are replaced with the cold modulus values, and the initial dimensions of the strained fixture elements are reduced due to thermal contraction during cooling.

$$\Delta s' = \Delta s(1 - \mathbf{e}_{\Delta Tsteel}) \quad (19)$$

$$\Delta y'_2 = \frac{\mathbf{s}_y Y'_{0copper}}{E_{copper}}, \quad Y'_{0copper} = Y_{0copper} (1 - \mathbf{e}_{\Delta Tcopper}) \quad (20)$$

$$\Delta y'_3 = \frac{\mathbf{s}_y Y'_{0steel}}{E_{steel}}, \quad Y'_{0steel} = Y_{0steel} (1 - \mathbf{e}_{\Delta Tsteel}) \quad (21)$$

$$\Delta y'_4 = \frac{\mathbf{s}_y Y'_{0top\_plate}}{E_{top\_plate}}, \quad Y'_{0top\_plate} = Y_{0top\_plate} (1 - \mathbf{e}_{\Delta Ttop\_plate}) \quad (22)$$

$$\Delta x'_{sample} = \frac{\mathbf{s}_x X'_{0sample}}{E_{sample}}, \quad X'_{0sample} = X_{0sample} (1 - \mathbf{e}_{\Delta Tsample}) \quad (23)$$

$$\Delta x'_{cap\_gauge} = \frac{\mathbf{s}_x X'_{0cap\_gauge}}{E_{cap\_gauge}}, \quad X'_{0cap\_gauge} = X_{0cap\_gauge} (1 - \mathbf{e}_{\Delta Tcap\_gauge}) \quad (24)$$

The new quantities employed in Equations 19-23 are listed in Table 2.

<i>Element</i>	$X_0 \mathbf{e} Y_0 \mathbf{e}$ (inches)	$E_{[T=4.2\text{ K}]}$ (MPa)
copper wedge	0.872	150,000
steel wedge	0.785	225,000
steel top plate	1.495	225,000
cap gauge	0.020	3,800
sample	0.573	varies

**Table 11** Essential quantities employed in the calculation of the fixture's vertical pre-stress at 4.2 K, including the fixture elements' initial dimensions following cool-down (but before deformation) and their cold modulus values.

Substituting  $\Delta x'_1$  for  $\Delta y'_1$  in Equation 14 by means of Equation 2, as in the derivation of the warm vertical stress model, we obtain the equation,

$$\Delta s(1 - \mathbf{e}_{\Delta Tsteel}) = \frac{1}{\tan \mathbf{q}} \left[ \frac{\mathbf{s}_x X'_{0sample}}{E_{sample}} + \frac{\mathbf{s}_x X'_{0cap\_gauge}}{E_{cap\_gauge}} + X_{0sample} \Delta \mathbf{e}_{\Delta Tsample} + X_{0cap\_gauge} \Delta \mathbf{e}_{\Delta Tcap\_gauge} \right] \quad (25)$$

$$+ \frac{\mathbf{s}_y Y'_{0copper}}{E_{copper}} + \frac{\mathbf{s}_y (Y'_{0steel} + Y'_{0top\_plate})}{E_{steel}} + Y_{0copper} \Delta \mathbf{e}_{\Delta Tcopper}$$

Given the geometric relation between the horizontal and vertical force in the system, defined by Equation 9, we next replace stress ( $\sigma$ ) with force (F) in Equation 25, by dividing out  $A_x = 0.457 \text{ inch}^2$  and  $A_y = 0.830 \text{ inch}^2$ , the reduced areas (following cool-down) over which  $F_x$  and  $F_y$  are distributed respectively. This yields the result:

$$\Delta s(1 - e_{\Delta T \text{ steel}}) = \frac{F_x}{A_x \tan \mathbf{q}} \left[ \frac{X'_{0\text{sample}}}{E_{\text{sample}}} + \frac{X'_{0\text{cap\_gauge}}}{E_{\text{kaptan}}} \right] + \frac{F_y}{A_y} \left[ \frac{Y'_{0\text{copper}}}{E_{\text{copper}}} + \frac{Y'_{\text{steel}} + Y'_{0\text{top\_plate}}}{E_{\text{steel}}} \right] \quad (26)$$

$$+ \frac{1}{\tan \mathbf{q}} (X_{0\text{sample}} \Delta e_{\Delta T \text{ sample}} + X_{0\text{cap\_gauge}} \Delta e_{\Delta T \text{ cap\_gauge}}) + Y_{0\text{copper}} \Delta e_{\Delta T \text{ copper}}$$

We use Equation 9 to express the equation entirely in terms of the force in the x-direction, and then collect all the force terms on one side of the equation, and all non-force dependent terms on the other.

$$\Delta s(1 - e_{\Delta T \text{ steel}}) - \frac{1}{\tan \mathbf{q}} (X_{0\text{sample}} \Delta e_{\Delta T \text{ sample}} + X_{0\text{cap\_gauge}} \Delta e_{\Delta T \text{ cap\_gauge}}) - Y_{0\text{copper}} \Delta e_{\Delta T \text{ copper}} =$$

$$F_x \left\{ \frac{1}{A_x \tan \mathbf{q}} \left[ \frac{X'_{0\text{sample}}}{E_{\text{sample}}} + \frac{X'_{0\text{cap\_gauge}}}{E_{\text{kaptan}}} \right] + \frac{1}{A_y \sin \mathbf{q} \cos \mathbf{q}} \left[ \frac{Y'_{0\text{copper}}}{E_{\text{copper}}} + \frac{Y'_{\text{steel}} + Y'_{0\text{top\_plate}}}{E_{\text{steel}}} \right] \right\} \quad (27)$$

Finally, after once again factoring in the pressurized area over which the vertical stress is distributed, and adding the fixture deformation correction factor as well as the experimental correction (which we extend directly from the warm vertical stress calibration), we are left, in Equation 28, with a well-defined model for the vertical pre-stress in the fixture as a function of shimming at  $T = 4.2 \text{ K}$ .

$$\mathbf{s}_{x\_cold} = \frac{\Delta s(1 - e_{\Delta T \text{ steel}}) - \frac{1}{\tan \mathbf{q}} (X_{0\text{sample}} \Delta e_{\Delta T \text{ sample}} + X_{0\text{cap\_gauge}} \Delta e_{\Delta T \text{ cap\_gauge}}) - Y_{0\text{copper}} \Delta e_{\Delta T \text{ copper}}}{\frac{1}{\tan \mathbf{q}} \left[ \frac{X'_{0\text{sample}}}{E_{\text{sample}}} + \frac{X'_{0\text{cap\_gauge}}}{E_{\text{kaptan}}} \right] + \frac{A_x}{A_y \sin \mathbf{q} \cos \mathbf{q}} \left[ \frac{Y'_{0\text{copper}}}{E_{\text{copper}}} + \frac{Y'_{\text{steel}} + Y'_{0\text{top\_plate}}}{E_{\text{steel}}} \right]} \left( \frac{0.8 - 1.5 \times 10^{-6} E_{\text{sample}}}{1 + \frac{E_{\text{sample}}}{E_{\text{steel}}}} \right)$$

*Application of the model:* Because of the inherent difficulties of performing a measurement at liquid helium temperature, it was not possible to carry out an extensive experimental calibration of the fixture's vertical stress mechanism at 4.2 K, as was done for the warm measurement. Nevertheless, the model expressed in Equation 28 for the fixture's cold vertical pre-stress is developed from a precise and effective model for the warm vertical pre-stress, which has been validated by abundant experimental evidence and, even further, proven its predictive power. The model for the fixture's cold vertical pre-stress is therefore a significant contribution to the understanding of mechanical dynamics in the fixture following cooling to 4.2 K and is a critical aid to the achievement of successful measurements in the cold bi-axial loading test.

The model predicts, for the G10 sample, with its given dimensions and characteristic values for  $E_{[T=300 \text{ K}]}$ ,  $E_{[T=4.2 \text{ K}]}$ , and  $\epsilon_{\Delta T}$ , a cold vertical pre-stress dependence on shimming of

$$\mathbf{s}_{cold} = -8263.7s + 662.43 \text{ MPa} \quad (29)$$

This dependence is plotted with the warm vertical pre-stress model in Figure 3, along with the derivative dependence of pre-stress change following cool-down  $\Delta \sigma_{\Delta T}$  upon the initial warm pre-stress in the fixture, which is defined, for the G10 sample, by

$$\Delta \mathbf{s}_{\Delta T} = +0.1853 \mathbf{s}_{warm} + 1.3307 \text{ MPa} \quad (30)$$

The first plot in Figure 3 shows that the cold vertical pre-stress is greater than the warm vertical pre-stress, in the case of the G10 sample, for all shim values. A gain in pre-stress, for the G10 sample, is therefore expected following cool-down from all warm pre-stresses, as the second plot illustrates, though the magnitude of the gain is dependent upon the magnitude of the initial pre-stress at room temperature. This result is caused by the fact that gains in pre-stress are determined by the marginal increase in modulus of the fixture's internal elements, between warm and cold temperatures, over the fixture's own modulus increase. This marginal modulus increase serves as a constant of proportionality between the

strains inside the fixture and the stresses associated with those strains; accordingly, the larger the initial strains imposed upon the elements inside the fixture by the initial pre-stress at room temperature, the larger the gain in pre-stress during cool-down, as determined by this constant of proportionality.

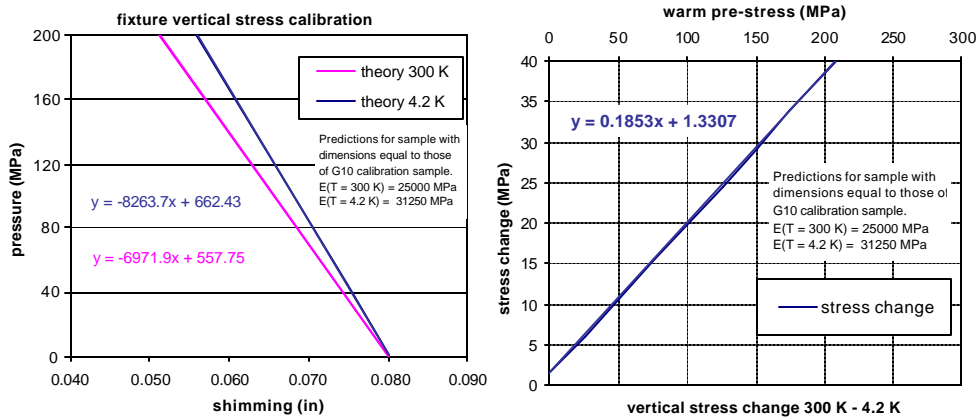


**Figure 3** Vertical pre-stress model plots for the G10 sample. The first graph is a comparison of vertical fixture pre-stresses, warm and cold, as a function of shimming, as predicted by Equations 10 and 28 in the discussion. The second plot shows the net change in pre-stress following cool-down, determined by the difference of the two models plotted in the first graph, as a function of initial warm vertical pre-stress. The G10 sample only gains pre-stress during cool down, because its integrated thermal contraction is less than that of the fixture.

Though G10 was the only sample tested in the cold bi-axial loading calibration, due to time constraints, it is of interest to consider the behavior of other samples during cooling on the basis of the model outlined in this appendix. In particular, in cases where the integrated thermal contraction of the sample is greater than that of the fixture, that is,  $\epsilon_{\Delta T \text{ sample}} > 3.05 \text{ mm/m}$ , as is expected for the cable ten-stack—which has an accepted value of  $\epsilon_{\Delta T} = 4.45 \text{ mm/m}$  (in the vertical direction) determined from previous measurements—the dynamics of cooling are more complicated. Because thermal contraction of the sample with respect to the fixture contributes to pre-stress loss rather than gain, the net change in pre-stress following cool-down is significantly sensitive to the initial pre-stress at room temperature.

Figures 4-7 explore the variable circumstances possible in the measurement of a potential cable ten-stack, whose moduli and integrated thermal contraction are much less strictly defined than for a calibration sample such as the G10.

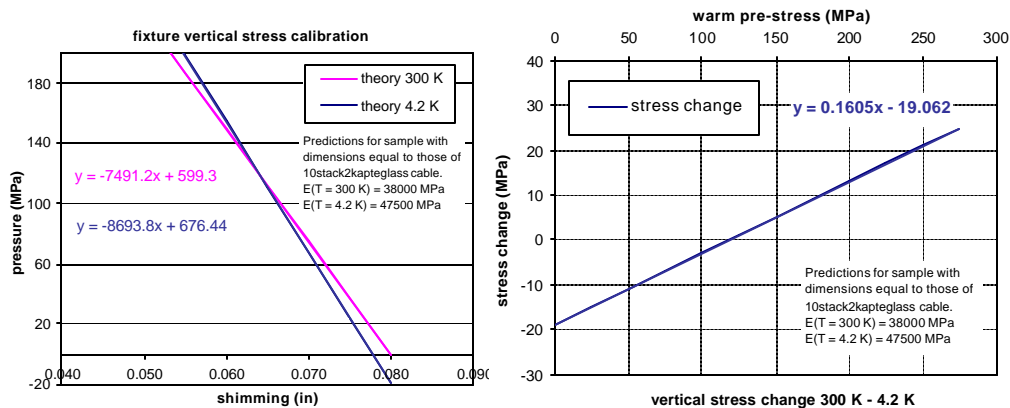


**Figure 4** Model plots for a hypothetical sample with dimensions of the latest cable ten-stacks, as well as thermo-mechanical variables used widely for the cables in magnet mechanical design models. Because the integrated thermal contraction of this sample is greater than that of the fixture, the direction of pre-stress change depends upon the initial warm pre-stress, unlike the G10 case. This is evident in the first graph from the fact that the warm and cold pre-stress lines cross at  $s = 0.065$ , causing the second graph to cross zero at  $\sigma_{\text{warm}} = 120 \text{ MPa}$ .

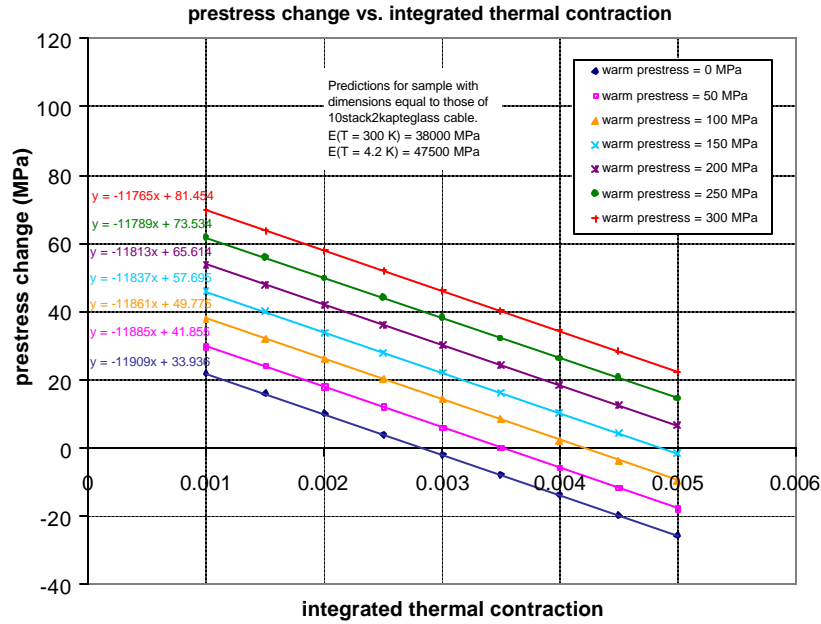


**Figure 5** Pre-stress change as a function of vertical-axis integrated thermal contraction for the hypothetical ten-stack cable. The plot illustrates well the general functional structure of the change in pre-stress due to cooling, with magnitudes dependent upon the initial warm pre-stress, and directionality dependent upon the sample’s integrated thermal contraction. If  $\epsilon_{\Delta T_{\text{sample}}} < \epsilon_{\Delta T_{\text{steel}}}$ , the fixture is almost exclusively likely to gain pre-stress following cool-down. If  $\epsilon_{\Delta T_{\text{sample}}} > \epsilon_{\Delta T_{\text{steel}}}$ , however, the direction of change depends upon the initial warm pre-stress of the fixture.

To generate the results plotted in Figures 4 and 5, we introduced some likely values for these variables into the model: an  $\epsilon_{\Delta T} = 4.45$  mm/m, an  $E_{[T=300\text{ K}]} = 38,000$  MPa, and an  $E_{[T=4.2\text{ K}]} = 47,500$  MPa; these are the values yielded by a previous measurement study for the vertical axis of the cable, and are the values employed in Ansis models when these parameters are required for calculating mechanical design features of the magnets. The model’s results confirm the physical intuition that the direction of pre-stress change becomes dependent upon initial warm pre-stress in the case of a sample with integrated thermal contraction less than that of the fixture.

Figures 6 and 7 investigate the change to the model for the same cable ten-stack if the ten-stack’s

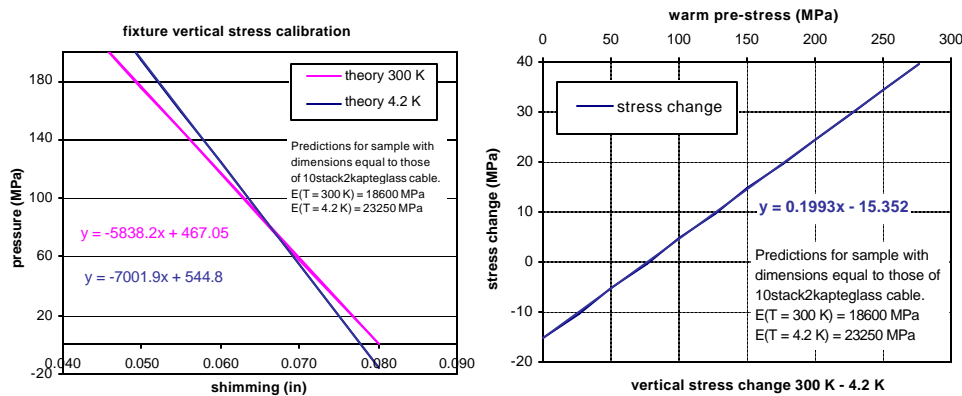


**Figure 6** Pre-stress loss model plots for a hypothetical cable with the same integrated thermal contraction as in Figures 4 and 5, but with moduli equal to approximately half the traditionally accepted value. The calibration slopes are proportionately reduced, though the cold pre-stress calibration is much less affected by the modulus change. As a result, the pre-stress change line in the second graph shifts vertically and its slope is increased, meaning smaller losses and larger gains in pre-stress are expected as a result of the reduction in the sample’s hypothetical modulus.

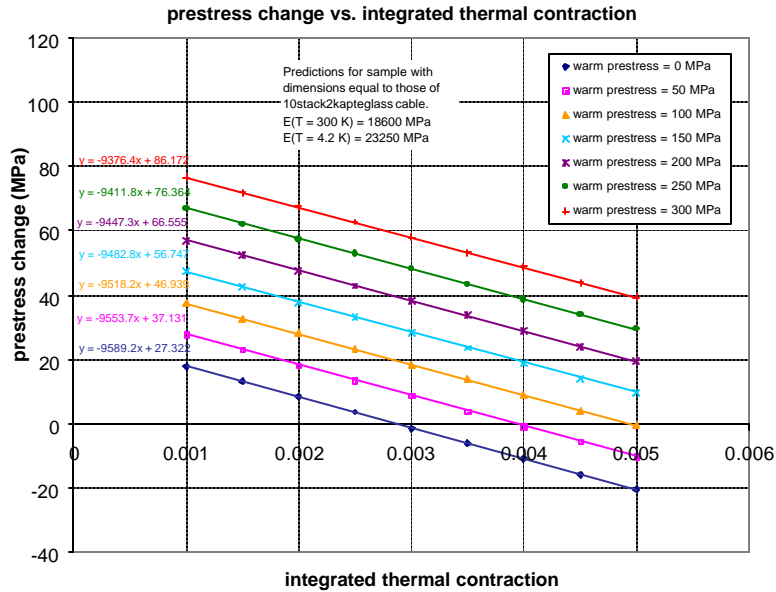


**Figure 7** Pre-stress change as a function of vertical axis integrated thermal contraction for the hypothetical ten-stack cable, with moduli equal to approximately half the traditionally accepted value. The general structure of the model remains the same, as can be seen from comparison of Figures 5 and 7. The pre-stress change’s dependence upon the sample’s integrated thermal contraction is relatively greater for the sample of higher modulus, as attested by the higher slopes in Figure 5, though the magnitude of the change is relatively greater for the sample of lower modulus, as is evident from the higher spacing (or intercepts) of the series in Figure 7 (this latter point is merely a repetition of the statements characterizing the second graph of Figure 6).

moduli are reduced by half from the traditionally accepted value. Such a possibility is plausible, because changes in cable insulation have a significant effect upon ten-stack modulus in the vertical direction. The basic structure of the model is unaffected by this change to the moduli of the hypothetical sample, though it is worth noting that the magnitude and rate of positive pre-stress change, with respect to initial warm pre-stress, is increased (see the second graph in Figure 6).

These results demonstrate good prospects for maintaining sufficient pre-stress during cool-down to support a cable ten-stack in the vertical direction for a loading test upon its horizontal axis, where it is mechanically weak if unsupported. So long as a  $\sigma_{\text{warm}} \geq 60\text{ MPa}$ , the sample should remain adequately supported following cool-down for a cold bi-axial measurement of its horizontal modulus—the ultimate aim of this measurement program. These prospects are shown to be even better for a cable ten-stack with a modulus lower than the traditionally accepted value of  $E_{\text{v\_cable}} = 38,000\text{ MPa}$ , since the intrinsic loss is less, and the rate of pre-stress gain as a function of warm pre-stress, is greater.